How Charge Carrier Exchange between Absorber and Contact Influences Time Constants in the Frequency Domain Response of Perovskite Solar Cells

Sandheep Ravishankar[1,*] Zhifa Liu,[1] Yueming Wang,[1] Thomas Kirchartz[1,2] and Uwe Rau[1]

[1]*IEK-5 Photovoltaik, Forschungszentrum Jülich, 52425 Jülich, Germany*

[2]*Faculty of Engineering and CENIDE, University of Duisburg-Essen, Carl-Benz-Str. 199, 47057 Duisburg, Germany*

A model is derived for the frequency and time domain optoelectronic response of perovskite solar cells (PSCs) that emphasizes the role of charge carrier exchange, i.e., extraction and injection, from (to) the perovskite through the transport layer to (from) the collecting electrode. This process is described by a charge carrier exchange velocity that depends on the mobility and electric field inside the transport layer. The losses implied by this process are modeled in an equivalent circuit model in the form of a voltage-dependent transport layer resistance. The analysis of the model predicts that the voltage dependence of the measured time constants allows discriminating situations where the transport layer properties dominate the experimental response. Application of this method to experimental impedance spectroscopy data identifies charge extraction velocities between 1 and 100 cm/s under 1-sun open-circuit conditions for *p-i-n* PSCs with poly(triaryl amine) as the hole transport layer; this corresponds to transport layer mobilities between 10^{-4} and 3×10^{-3} cm^2 V^{-1} s^{-1}. The model paves the way for an accurate estimation of the photocurrent and fill factor losses in PSCs caused by low mobilities in the transport layers, using small-perturbation measurements in the time and frequency domain.

I. INTRODUCTION

The analysis of different fundamental working mechanisms in perovskite solar cells (PSCs) is largely carried out using a suite of time domain and frequency domain optoelectronic techniques. These techniques generally involve the measurement of the response of the solar cell or stack to a perturbation of the photon flux, ϕ; the external voltage, V_{ext}; or the current density, j. In the time domain, these techniques include transient photovoltage (TPV), transient photocurrent (TPC), and transient photoluminescence (TRPL) measurements. While TPV and TPC measure the external voltage and current density, respectively, to a small perturbation of light intensity, TRPL measures the emitted photon flux to a large perturbation of light intensity. The analysis of these measurements typically involves the fitting of the rise or decay of the measured quantity using a mono- or biexponential fit [1–4], subsequently assigning the calculated time constant to a physical process, such as recombination or transport.

However, as shown using drift-diffusion simulations, such an analysis is almost always an oversimplification of a situation where several mechanisms can coexist, superimpose, and vary in relative importance as a function of illumination and bias conditions, structure (device or stack), and material properties [5,6]. For example, a comparison of lifetimes obtained from TRPL (usually measured on stacks) and TPV (measured on devices) measurements show that the TPV lifetimes are generally a few orders higher due to measurement of the geometric capacitance-dominated region of the apparent lifetime [7,8]. In this regard, in the case of TPV and TRPL, the definition of a differential decay time at each point of the decay in addition to conversion of the time axis to an open-circuit voltage (V_{OC}) axis allows easier discrimination of physical mechanisms, facilitating comparison of the different device structures and between the two methods.

In the case of the frequency domain, the corresponding counterparts for TPV and TPC are intensity-modulated photovoltage spectroscopy (IMVS) and intensity-modulated photocurrent spectroscopy (IMPS), respectively, while impedance spectroscopy (IS) measures the modulated current density upon the application of a modulated external voltage. Recent work using these methods has focused on combining the information contained within each of them to obtain a unified interpretation, in the form of a single equivalent circuit [9,10] or through the

application of the diffusion-recombination model [11,12]. While equivalent circuits allow easier modeling and analysis of overlapping physical mechanisms compared to the time domain methods, it is still unclear which equivalent circuit reliably models a wide range of PSCs.

However, the biggest concern in the interpretation of both time domain and frequency domain spectra is the nonaccounting of nonlinear transport layer effects. While the perovskite is known to be an efficient transporter of charge due to its large electron and hole mobilities (mobility > 1 cm^2 V^{-1} s^{-1}) [13], the transport layers are much less efficient in comparison. Furthermore, due to their low thickness, often low permittivity, and typically also low conductivity, they do not behave like a simple series resistance that could easily be implemented into an equivalent circuit. This is especially the case for *p-i-n* PSCs, which employ thin organic layers, such as poly(triaryl amine) (PTAA), [6,6]-phenyl-C$_{61}$ butyric acid methyl ester (PCBM), C$_{60}$-fused *N*-methylpyrrolidine-*m*-C$_{12}$-phenyl (CMC), and indene-C$_{60}$ bisadduct (ICBA) [14], with comparatively lower mobilities between 10^{-5} and 10^{-2} cm^2 V^{-1} s^{-1} [15–17]. This means that the effective response in a measurement can contain contributions from, or even be dominated by, the response of the transport layers, as we have shown recently for different capacitance-based methods used to investigate PSCs [18–20]. In such cases, the measured response and hence the calculated parameters are wholly and wrongly attributed to that of the perovskite layer. In addition, recent studies have shed light on the existence of an internal series resistance in any illuminated solar cell in general [21,22]. This series resistance is a function of the external voltage and models the translation of the internal voltage, V_{int}, to the voltage, V_{ext}, at the electrodes, which is required to drive the current density from the bulk to the outer circuit [23]. In the case of PSCs, this resistance is the chemical potential drop in the transport layer (termed the transport layer resistance) and is a function of the mobility of the transport layer and the electric field inside it [18]. Therefore, a new model that accounts for this transport layer resistance and decouples the response of charge extraction and transport in the transport layers from that of recombination in the perovskite layer is required to model the time and frequency domain spectra of PSCs more effectively.

Here, we solve this problem through the development of a model that is applicable to small-perturbation measurements of any solar cell that consists of a high mobility absorber layer in series with charge transport layers of variable mobility. In addition to encompassing the fundamental mechanisms of charge generation, recombination, and capacitive discharge, this model explicitly accounts for the difference in the internal and external voltages and the associated charge carrier transfer between the bulk and the electrodes, in the form of an injection or extraction

velocity, S_{exc}. This injection or extraction velocity depends on the electric field and the mobility of the majority carriers in the charge transport layers. The model predicts the voltage dependence of the measured time constants and their corresponding resistances and capacitances, which can be exploited to discriminate between the overlapping mechanisms of recombination in the perovskite layer and charge extraction and transport in the transport layers. Analysis of experimental IS measurements of PSCs with different transport layers using this method identifies that the high-frequency resistance of PTAA-based PSCs at open-circuit voltages under 1 sun is dominated by the transport layer resistance. This yields charge carrier exchange velocities between 1 and 100 cm/s under 1-sun open-circuit conditions, which corresponds to transport layer mobilities between 10^{-4} and 3×10^{-3} cm^2 V^{-1} s^{-1} for the PTAA-based PSCs.

Thus, our developed model allows a deep analysis of the loss mechanisms in the PSC and calculation of their corresponding key parameters, such as the Shockley-Read-Hall (SRH) lifetime, the charge extraction velocity, and the transport layer mobility. In particular, the latter parameters are fundamental for state-of-the-art high-efficiency PSCs because they strongly contribute to losses in the fill factor of its current-voltage curve. Furthermore, this model is universally applicable to any electrical or luminescence technique in the time or frequency domain.

II. EXPERIMENTAL SPECTRA

IS measurements are performed on a range of *p-i-n* PSCs under open-circuit conditions. These PSCs show efficiencies between 15% and 20% and consist of different compositions of the perovskite layer and different electron and hole transport layers (ETL and HTL, respectively), as summarized in Table S1 within the Supplemental Material [48] (see Sec. A1 for experimental details and Fig. S1 within the Supplemental Material [48] for current-voltage curves). These include PTAA and self-assembled monolayers (SAMs) of [2-(9H-Carbazol-9-yl)ethyl] phosphonic acid (2PACz) and (4-(3,6-dimethyl-9H-carbazol-9-yl)butyl) phosphonic acid (Me-4PACz) for the HTL and PCBM/bathocuproine (BCP), PCBM:CMC:ICBA/BCP, and C$_{60}$/BCP for the ETL. These devices show good stability during the measurements, with a maximum of only 4–5-mV dc open-circuit voltage loss after the measurement at the highest light intensity.

The Nyquist (real vs imaginary part of the transfer function) plots from these measurements generally yield two arcs (as shown in Fig. S2 within the Supplemental Material [48]), one at high frequencies above 10^4 Hz and one at low frequencies in the region of a few hundred Hz to mHz. Under large open-circuit voltages, a third arc at low frequencies is observed. For the case of frequency domain measurements, the PSC response above approximately

10^3 Hz is considered to be purely electronic in nature [24]. However, conductivity measurements on perovskite pellets and films have calculated ionic transport frequencies (and hence, ion-dominated response) of approximately 10^5 Hz and below [25,26]. While the discrepancy in the values between frequency domain measurements and conductivity measurements is not well understood, we assume that frequencies of 10^4 Hz and above (i.e., high-frequency arc in the IS spectrum) are dominated by purely electronic phenomena.

Figure 1(a) shows the measured high-frequency time constant and its evolution versus open-circuit voltage. At large open-circuit voltages close to the 1-sun open-circuit voltage, a constant value of the time constant is observed, between 2×10^{-7} and 2×10^{-6} s. At lower open-circuit voltages, this plateau transitions into an exponentially increasing time constant with reducing open-circuit voltage. For comparison, the measured time constants of a PSC from a TRPL measurement of a high-performance Methylammonium lead iodide (MAPI) PSC is shown [27], which follows a similar exponential increase at lower open-circuit voltages, followed by a plateau, and then an exponential decrease with increasing open-circuit voltage, forming an "S" shape. The IS time constants follow a similar S shape but do not show the exponential drop in the time constant due to the inability to reach such large values of open-circuit voltage compared to the TRPL measurement. We clarify that the comparison of time constants obtained

from frequency domain methods and luminescence methods on the same device is justified by the fact that both methods measure the decay of an excess charge carrier density, Δn, via an emitted photon flux, a current or a voltage that is measured. The rise or decay of these quantities is then assigned a characteristic time constant using analysis methods that depend on the type of measurement being made. However, the decay of the excess charge carrier density is governed by the fundamental physical processes of recombination, diffusion, charge extraction, etc., irrespective of the type of measurement. In the simplest case of an infinitely thick absorber and perfectly injecting or extracting contacts, we thus expect the measured time constants from both electrical and luminescence methods to correspond to the recombination lifetime.

The corresponding resistances and capacitances that form the IS time constants are shown in Figs. 1(b) and 1(c) respectively. The resistance decreases exponentially followed by either an increased slope or saturation at large open-circuit voltages, while the capacitance shows saturation at lower open-circuit voltages followed by an exponential increase at larger open-circuit voltages. We note that the resistances change over several orders of magnitude compared to the capacitances, which means the evolution of the time constant is dominated by the resistances. The plateau region in the time constants is usually interpreted as originating from a first-order recombination process coupled with the chemical capacitance (which leads to a voltage-independent lifetime), associated
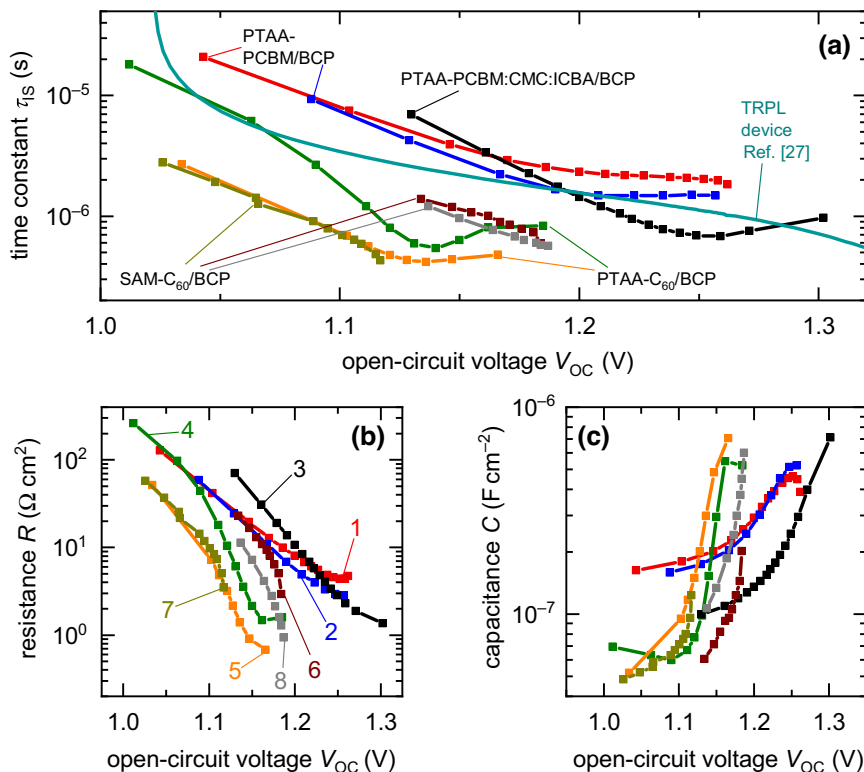

FIG. 1. Measured (a) high-frequency time constant and corresponding (b) resistance and (c) capacitance from IS measurements at different open-circuit voltages, on different *p-i-n* PSCs (see Table S1 in the Supplemental Material [48] for a summary of sample data and Fig. S1 within the Supplemental Material [48] for current-voltage curves). Also shown in (a) using a line with no symbols is the differential lifetime obtained from a TRPL measurement of a MAPI PSC, reproduced with permission from Ref. [27]. Labels in (a) indicate the HTL and ETL layers of the cell in the format "HTL-ETL." Labels in (b) show the numbers corresponding to each sample (see Table S1 in the Supplemental Material [48]) used as a reference. Light source used for the IS measurements is a blue light-emitting diode (LED) centered at 482 nm.

with either nonradiative recombination in the bulk (τ_{SRH}), radiative recombination under low injection conditions with bulk doping density N_{D} ($\tau = 1/B_{\text{rad}}N_{\text{D}}$), or surface recombination [5]. The exponential increase in the time constant at lower open-circuit voltages is found to originate from the coupling of the discharge of the geometric capacitance to the recombination [5,7,8,28]. The influence of a more general dielectric capacitance on the measured lifetimes was discussed in Ref. [29]. However, these interpretations are not sufficient to explain the data, as the IS measurement is also sensitive to the transport layer resistances due to the modulated current density flowing in or out of the cell and is hence strongly affected by them. This logic is given further credence by the saturation of the resistances in Fig. 1(b), which is not typical of any recombination mechanism, since a recombination resistance scales versus voltage as $\exp(-qV_{\text{int}}/n_{\text{id}}k_{\text{B}}T)$, with $n_{\text{id}} = 1$ for radiative recombination and $n_{\text{id}} = 2$ for nonradiative recombination via deep traps in an intrinsic layer [18,30]. Therefore, there is a fundamental need for an advanced model of the PSC that incorporates the direct and indirect effects of the transport layers on its transient response, that is derived in the next section.

III. THEORY

A. Charge carrier exchange between absorber and contact

We begin by assuming a thin-film PSC with an intrinsic perovskite absorber of thickness d in contact with an ETL at $x = 0$ of thickness d_{TL} and a perfectly blocking contact for electrons at $x = d$. We further assume that the electric field inside the perovskite layer is negligible due to shielding by the ions and that the diffusion length is much larger than the thickness of the perovskite layer (a valid assumption for thin-film PSCs [13]), implying a constant and equal density of electrons and holes within it, given by

$$np = n^2 = n_i^2 \exp\left(\frac{qV_{\text{int}}}{k_{\text{B}}T}\right) \rightarrow n = n_i \exp\left(\frac{qV_{\text{int}}}{2k_{\text{B}}T}\right), \quad (1)$$

where n_i is the intrinsic carrier concentration and $V_{\text{int}} = (E_{\text{F}n} - E_{\text{F}p})/q$ represents the steady-state splitting of the quasi-Fermi levels $E_{\text{F}n}$ ($E_{\text{F}p}$) of electrons (holes) inside the absorber layer. Assigning the split of the quasi-Fermi levels to an internal voltage, V_{int}, is helpful, but we have to bear in mind that this internal "voltage" is not a voltage in the sense of an *electrostatic* potential, rather it expresses the sum of the excess *chemical* potentials of electrons and holes. The steady-state current, j, through the device, in the traditional formalism, is given by

$$j = j_{\text{SC}} - j_0\left(\exp\left(\frac{qV_{\text{elec}}}{n_{\text{id}}k_{\text{B}}T}\right) - 1\right), \quad (2)$$

where j_{SC} is the short-circuit current density, j_0 is the reverse saturation current density, n_{id} is the ideality factor, and V_{elec} is the steady-state quasi-Fermi level of the electrons at the cathode minus the quasi-Fermi level of the holes at the anode. Equation (2) connects the current density, j, to the applied external voltage by assuming that the splitting of the quasi-Fermi levels equals the voltage, V_{elec}, i.e., $V_{\text{int}} = V_{\text{elec}}$. Equation (2) is the basis of the superposition principle—adding the photogenerated current to the dark recombination current to produce the current-voltage curve under illumination.

However, while $V_{\text{int}} = V_{\text{elec}}$ might be a good approximation at open circuit, it is never a good approximation for V_{elec} significantly smaller than V_{OC}. The need to drive current out of a device leads to deviations from the superposition principle that become visible in the form of variations in recombination current under dark and illumination conditions [22,31], with large luminescence observed under short-circuit conditions for silicon [32], Cu(In, Ga)Se_2 (CIGS) [23], organic solar cells [33], and perovskite solar cells [22,34]. These findings imply large quasi-Fermi level splitting inside the absorber layer under illumination followed by a drop to qV_{elec}, which can occur either inside the space-charge region (as in silicon or CIGS solar cells) or within the transport layers (as in perovskite solar cells). The current density in the PSC thus depends on both V_{int} and V_{elec}, given by [18]

$$j_{\text{exc}} = j_{\text{B}}\left[\exp\left(\frac{qV_{\text{int}}}{2k_{\text{B}}T}\right) - \exp\left(\frac{qV_{\text{elec}}}{2k_{\text{B}}T}\right)\right]. \quad (3)$$

Prefactor j_{B} is a reference current density that controls the efficacy of charge carrier exchange between the absorber and external terminal of the device. Corresponding analogues of Eq. (3) were derived for single-sided p-n junctions in Ref. [23] and using an alternative equivalent circuit model in Ref. [21]. We note that a positive value of j_{exc} in Eq. (3) implies $V_{\text{int}} > V_{\text{elec}}$, corresponding to the situation where a current is driven out of the solar cell under illumination, with $V_{\text{elec}} = V_{\text{ext}} + j_{\text{exc}}R_{\text{s}}$, where V_{ext} is the applied external voltage and R_{s} is the series resistance.

Equation (3) assumes symmetry between the behavior of electrons and holes, where the exchange current, j_{exc}, is the same at the electron contact and at the hole contact [Fig. 2(a)]. While prefactor j_{B} is voltage independent in p-n junctions [23], it becomes voltage dependent in the case of undoped electron and hole transport layers over which a significant electric field drops. If the electric field is approximately constant over the transport layers, an analytical solution for j_{B} exists, as given by

$$j_{\text{B}} = \frac{q\mu_{\text{TL}}F_{\text{TL}}n_i\exp(q\Phi_{\text{b,pero}}/k_{\text{B}}T)}{1 - \exp(-(qF_{\text{TL}}d_{\text{TL}}/k_{\text{B}}T))} = qn_{\text{int}}S_{\text{exc}}(V_{\text{elec}}),$$
$$(4)$$

which is consistent with the derivations found in Ref. [35]. In Eq. (4), μ_{TL} is the mobility of electrons in the ETL and $n_{\text{int}} = n_i\exp(q\Phi_{\text{b,pero}}/k_{\text{B}}T)$ is the electron concentration at the interface between the perovskite and the ETL, with n_i being the intrinsic concentration in the perovskite absorber and $q\Phi_{\text{b,pero}}$ the band offset for electrons at the perovskite-ETL interface. F_{TL} is the electric field in the transport layer, which is given by (under the assumption of a constant electric field)

$$F_{\text{TL}} = \frac{(V_{\text{BI,TL}} - (V_{\text{elec}}/k))}{d_{\text{TL}}}, \quad (5)$$

where $V_{\text{BI,TL}}$ is the built-in electrostatic potential difference in the transport layer and k is a factor that controls the amount of the electrode voltage that goes to the transport layer, i.e., $k = 2$ for the symmetric case [cf. Fig. 2(a)]. S_{exc} is an exchange velocity, which, within the validity range of Eq. (4), is given by [35]

$$S_{\text{exc}}(V_{\text{elec}}) = \frac{\mu_{\text{TL}}F_{\text{TL}}}{1 - \exp(-(qF_{\text{TL}}d_{\text{TL}}/k_{\text{B}}T))}. \quad (6)$$

S_{exc} is a function of mobility μ_{TL} and electric field F_{TL} in the transport layer that determines the magnitude of the gradient in electrochemical potential required to sustain the current flow through the device. A factor similar to Eq. (6) was derived in Ref. [36] for the current density in organic light-emitting diodes. We note that Eq. (3) is an alternative representation (see Sec. A2 in the Supplemental Material [48] for derivation) of the formula derived in the Supporting Information of Ref. [18]. In addition, Table S2 within the Supplemental Material [48] summarizes all the parameters that are used in this paper.

B. Small-perturbation model

Now we turn to the overall balance of charge carriers in the perovskite absorber. Based on the large reported electronic diffusion coefficients, D, in a typical thin-film perovskite of thickness $d = 300$ nm, we expect a diffusion frequency of $f_{\text{diff}} = D/d^2 \cong 1000$ MHz (assuming $D = 1$ cm²/s, as reported in Refs. [37,38]). Such values are well above the maximum frequency of perturbation in typical frequency domain measurement setups; hence, we should not be able to see any diffusion or diffusion-related effects, such as a source wavelength dependence in the measured spectra. The model therefore uses the assumption that diffusion of electronic carriers within the typical thin-film perovskite is fast enough to assume that the dc and ac concentrations of electronic carriers are uniform within the thickness of the perovskite layer (a list of assumptions made in the development of the model is shown in Fig. S4 within the Supplemental Material [48]). Based on this assumption, we may describe the total amount of electrons in the absorber by concentration n multiplied by absorber thickness d. Thus, the balance of electrons in the absorber is given by photogeneration and recombination and by the extraction (injection) of electrons to (from) the contact according to

$$\frac{dn}{dt} = -\frac{j_{\text{exc}}}{qd} + \frac{j_{\Phi}}{qd} - \frac{n}{\tau_{\text{SRH}}} - B_{\text{rad}}n^2, \quad (7)$$

where j_{Φ} is the input photon flux multiplied by the elementary charge q that corresponds to the generation rate, τ_{SRH} is the lifetime corresponding to bulk Shockley-Read-Hall (SRH) recombination via deep traps, and B_{rad} is the radiative recombination coefficient (cm³/s). We assume equal electron and hole densities and negligible detrapping rates to obtain a first-order SRH recombination rate with lifetime $\tau_{\text{SRH}} = \tau_{\text{n}} + \tau_{\text{p}}$, where τ_{n} and τ_{p} are the SRH lifetimes of electrons and holes. A schematic of the different processes considered in the model is shown in Fig. 2(a). Note that, for simplicity, we omit recombination at the interfaces between the absorber and transport layers. Since our model assumes deep traps, surface recombination depends linearly on the charge carrier concentration, n, with lifetime $\tau_{\text{int rec}} = d_{\text{pero}}/S_{\text{int rec}}$, where $S_{\text{int rec}}$ is the surface recombination velocity [5]. Furthermore, since our model assumes flat Fermi levels, surface recombination is in parallel to bulk SRH recombination to yield an effective SRH lifetime of $\tau_{\text{eff,SRH}} = (1/\tau_{\text{SRH}} + 1/\tau_{\text{int rec}})^{-1}$. Thus, the omission of surface recombination does not have any implications for the analysis of the model, since surface recombination can be accounted for by simply considering τ_{SRH} as $\tau_{\text{eff,SRH}}$, the parallel combination between the bulk SRH and surface recombination lifetimes.

Now we turn to the linearized small-signal analysis of Eq. (7), using small-perturbation quantities as symbols with a tilde. For simplicity, we assume no band offset at the perovskite-transport layer interface, i.e., $n_{\text{int}} = n_i$. Applying a small perturbation to Eqs. (3) and (7), using Eq. (1) and removing steady-state terms, we obtain

$$\begin{aligned} \frac{d\tilde{n}}{dt} &= -\left[\frac{1}{\tau_{\text{SRH}}} + \frac{1}{\tau_{\text{rad}}}\right]\tilde{n} - \frac{1}{qd}\left[\frac{dj_{\text{exc}}}{dV_{\text{elec}}}\tilde{V}_{\text{elec}} + \frac{dj_{\text{exc}}}{dn}\tilde{n}\right] + \frac{\tilde{j}_{\phi}}{qd}, \\ &= -\frac{\tilde{n}}{\tau_{\text{eff}}} - \frac{1}{qd}\left[\frac{\tilde{V}_{\text{elec}}}{R_{\text{exc}}} + S_{\text{exc}}\tilde{n}\right] + \frac{\tilde{j}_{\phi}}{qd}, \end{aligned} \quad (8)$$

where τ_{eff} is the effective recombination lifetime given by the parallel combination of the SRH lifetime and radiative lifetime $\tau_{\text{rad}} = 1/(2B_{\text{rad}}n)$. To rewrite Eq. (8) for the time derivative of the modulated internal voltage, $\tilde{V}_{\text{int}}$, we use Eq. (1) to obtain

$$\tilde{n} = \left(\frac{dn}{dV_{\text{int}}}\right)\tilde{V}_{\text{int}} = \frac{qn_i}{2k_{\text{B}}T}\exp\left(\frac{qV_{\text{int}}}{2k_{\text{B}}T}\right)\tilde{V}_{\text{int}} = \frac{C_{\mu}}{qd}\tilde{V}_{\text{int}}, \quad (9)$$
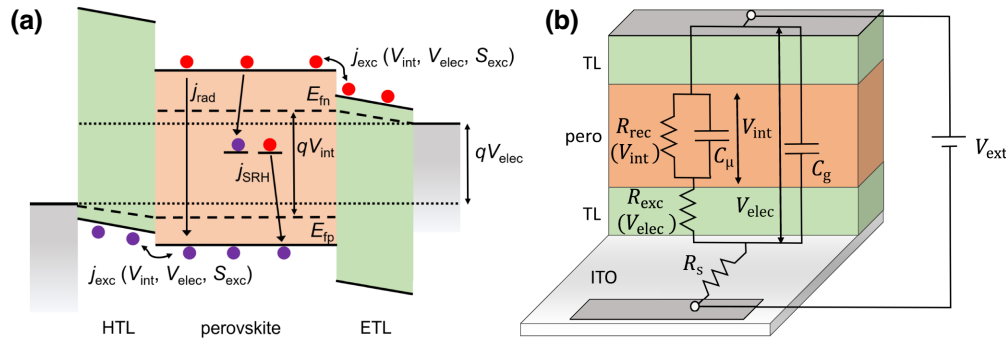
FIG. 2. (a) Schematic of physical mechanisms (represented as current densities j) that are considered in the model. We consider a symmetric device with equal exchange velocity S_{exc} for both transport layers. j_{rad} is the radiative recombination current density and j_{SRH} is the Shockley-Read-Hall nonradiative recombination current density. Electrons and holes are represented as red and purple spheres, respectively. V_{int} is the quasi-Fermi level splitting inside the perovskite layer and V_{elec} is the quasi-Fermi level of the electrons at the cathode minus the quasi-Fermi level of the holes at the anode. (b) Equivalent circuit derived from the model (see Sec. A4 in the Supplemental Material [48] for derivation). The exchange resistance R_{exc} models the potential drop across both the transport layers that translates the quasi-Fermi level splitting in the perovskite V_{int} to V_{elec}. R_{exc} itself depends on V_{elec} and the exchange velocity S_{exc}.

with the definition of the chemical capacitance, C_μ, given by [39]

$$C_\mu = qd\left(\frac{dn}{dV_{int}}\right) = \frac{q^2 dn_i}{2k_B T}\exp\left(\frac{qV_{int}}{2k_B T}\right). \quad (10)$$

With this, we obtain

$$C_\mu \frac{d\tilde{V}_{int}}{dt} = -\frac{\tilde{V}_{int}}{R_{rec}} - \left[\frac{dj_{exc}}{dV_{elec}}\tilde{V}_{elec} + \frac{dj_{exc}}{dV_{int}}\tilde{V}_{int}\right] + \tilde{j}_\phi. \quad (11)$$

Under open-circuit bias conditions, we have $V_{elec} = V_{int}$ and therefore

$$-\frac{dj_{exc}}{dV_{elec}} = \frac{dj_{exc}}{dV_{int}} = \frac{1}{R_{exc}}, \quad (12)$$

which implies for the exchange resistance that

$$R_{exc} = \frac{2k_B T}{qj_B(V_{elec})}\exp\left(-\frac{qV_{elec}}{2k_B T}\right) = \frac{2k_B T}{qj_B(V_{int})}$$

$$\exp\left(-\frac{qV_{int}}{2k_B T}\right). \quad (13)$$

Thus, Eq. (8) transforms into

$$C_\mu \frac{d\tilde{V}_{int}}{dt} = -\frac{\tilde{V}_{int}}{R_{rec}} + \frac{\tilde{V}_{elec}}{R_{exc}} - \frac{\tilde{V}_{int}}{R_{exc}} + \tilde{j}_\phi, \quad (14)$$

with the recombination resistance, R_{rec}, given by

$$\begin{aligned}
R_{rec} &= \frac{\tau_{eff}}{C_\mu} = \left(\frac{1}{R_{rec,SRH}} + \frac{1}{R_{rec,rad}}\right)^{-1}, \\
&= \Bigg[\frac{1}{(2k_B T\tau_{SRH}/q^2 dn_i)\exp(-(qV_{int}/2k_B T))} \\
&\quad + \frac{1}{(k_B T/q^2 dn_i^2 B_{rad})\exp(-(qV_{int}/k_B T))}\Bigg]^{-1},
\end{aligned} \quad (15)$$

where $R_{rec,SRH}$ and $R_{rec,rad}$ are the nonradiative and radiative recombination resistances, respectively. Finally, we consider the time development of the small-signal external voltage, $\tilde{V}_{elec}$, taking into account that this voltage builds up over geometric capacitance C_g. The charge needed to build up this voltage stems from the current leaving the absorber and the electrical current, $\tilde{j}_{elec}$, from the outer circuit, leading to

$$C_g \frac{d\tilde{V}_{elec}}{dt} = -\frac{\tilde{V}_{elec}}{R_{exc}} + \frac{\tilde{V}_{int}}{R_{exc}} - \tilde{j}_{elec}. \quad (16)$$

C. Matrix equations (dc open-circuit conditions)

At this point, it is convenient to put the time development of both voltages $\tilde{V}_{int}$ and $\tilde{V}_{elec}$ into a matrix equation. We thus have

$$\begin{pmatrix} C_\mu & 0 \\ 0 & C_g \end{pmatrix}\begin{pmatrix} (d/dt)\tilde{V}_{int} \\ (d/dt)\tilde{V}_{elec} \end{pmatrix}$$

$$= \begin{pmatrix} -\frac{1}{R_{exc}} - \frac{1}{R_{rec}} & \frac{1}{R_{exc}} \\ \frac{1}{R_{exc}} & -\frac{1}{R_{exc}} \end{pmatrix}\begin{pmatrix} \tilde{V}_{int} \\ \tilde{V}_{elec} \end{pmatrix} + \begin{pmatrix} \tilde{j}_\phi \\ -\tilde{j}_{elec} \end{pmatrix}. \quad (17)$$

In Eq. (17), all small-signal quantities depend on time, and all dc parameters are calculated under open-circuit conditions. The excitation can be chosen to be $\tilde{j}_\phi = j_{\Phi,0} \times \delta(0)$, where $j_{\Phi,0}$ is a prefactor and $\delta(0)$ is a Dirac-Delta function centered at $t = 0$, and $\tilde{j}_{elec} = 0$ to describe the transient of the photovoltage (IMVS), $\tilde{V}_{elec}(t)$, following delta excitation by a light pulse. Similarly, we may calculate the time transient of the internal voltage, $\tilde{V}_{int}$, i.e., of the chemical potential, to describe the transient photoluminescence (TRPL); see also Ref. [40].

When turning to frequency domain measurements, we interpret Eq. (17) as an equation for complex-valued small-signal quantities by replacing the time derivative with the angular frequency, ω, with the imaginary unit, i, leading to

$$i\omega \begin{pmatrix} C_\mu & 0 \\ 0 & C_g \end{pmatrix} \begin{pmatrix} \tilde{V}_{int}(\omega) \\ \tilde{V}_{elec}(\omega) \end{pmatrix} = \begin{pmatrix} -\frac{1}{R_{exc}} - \frac{1}{R_{rec}} & \frac{1}{R_{exc}} \\ \frac{1}{R_{exc}} & -\frac{1}{R_{exc}} \end{pmatrix}$$
$$\times \begin{pmatrix} \tilde{V}_{int}(\omega) \\ \tilde{V}_{elec}(\omega) \end{pmatrix} + \begin{pmatrix} \tilde{j}_\phi(\omega) \\ -\tilde{j}_{elec}(\omega) \end{pmatrix}. \tag{18}$$

Analogously to the use of Eq. (17) in the time domain, Eq. (18) can be used to describe different experimental methods in the frequency domain. For example, using a periodic excitation of the chemical potential by photogeneration $\tilde{j}_\phi = \tilde{j}_\phi(\omega)$ and keeping the sample under ac open-circuit conditions ($\tilde{j}_{elec} = 0$) would yield the signal $\tilde{V}_{elec}(\omega)$ as a solution of Eq. (18), to obtain the IMVS transfer function $W = \tilde{V}_{elec}(\omega)/\tilde{j}_\phi(\omega)$. Likewise, keeping the ac voltage at zero ($\tilde{V}_{elec} = 0$) and detecting instead $\tilde{j}_{elec} = \tilde{j}_{elec}(\omega)$ yields the IMPS transfer function $Q = \tilde{j}_{elec}(\omega)/\tilde{j}_\phi(\omega)$. We may also consider an excitation of the voltage $\tilde{V}_{elec}(\omega)$ without any periodic optical excitation ($\tilde{j}_\phi = 0$) and detect the response $\tilde{j}_{elec} = \tilde{j}_{elec}(\omega)$ of the electrical current, to obtain the IS transfer function $Z = \tilde{V}_{elec}(\omega)/\tilde{j}_{elec}(\omega)$. However, for the last two experimental methods, we need to consider an additional series resistance, R_s, in the complete equivalent circuit [shown in Fig. 2(b)], which slightly modifies the simple matrix Eqs. (17) and (18).

The relationships between the applied external voltage, V_{ext}, and the voltage at the electrodes, V_{elec}, is given using the external series resistance, R_s, as

$$\tilde{V}_{elec} = \tilde{V}_{ext} + R_s \tilde{j}_{elec}. \tag{19}$$

Substituting Eq. (19) into Eqs. (14) and (16), we obtain

$$\tilde{j}_\Phi + \frac{R_s}{R_{exc}} \tilde{j}_{elec} = \left[\frac{d}{dt} + \frac{1}{C_\mu} \left(\frac{1}{R_{exc}} + \frac{1}{R_{rec}} \right) \right] C_\mu \tilde{V}_{int}$$
$$- \frac{\tilde{V}_{ext}}{R_{exc}}, \tag{20}$$

$$\tilde{j}_{elec} \left(1 + \frac{R_s}{R_{exc}} + C_g R_s \frac{d}{dt} \right) = \frac{\tilde{V}_{int}}{R_{exc}} - \left(\frac{1}{R_{exc}} + C_g \frac{d}{dt} \right) \tilde{V}_{ext}. \tag{21}$$

Combining the frequency domain versions ($d/dt \to i\omega$) of Eqs. (20) and (21) and rearranging terms, we can obtain the matrix equations corresponding to different frequency domain techniques under dc open-circuit condition as follows.

For IMVS,

$$i\omega \begin{pmatrix} C_\mu & 0 \\ 0 & C_g \end{pmatrix} \begin{pmatrix} \tilde{V}_{int}(\omega) \\ \tilde{V}_{ext}(\omega) \end{pmatrix} = \begin{pmatrix} -\frac{1}{R_{exc}} - \frac{1}{R_{rec}} & \frac{1}{R_{exc}} \\ \frac{1}{R_{exc}} & -\frac{1}{R_{exc}} \end{pmatrix}$$
$$\times \begin{pmatrix} \tilde{V}_{int}(\omega) \\ \tilde{V}_{ext}(\omega) \end{pmatrix} + \begin{pmatrix} \tilde{j}_\Phi(\omega) \\ 0 \end{pmatrix}. \tag{22}$$

For IMPS,

$$i\omega \begin{pmatrix} C_\mu & 0 \\ 0 & C_g R_s \end{pmatrix} \begin{pmatrix} \tilde{V}_{int}(\omega) \\ \tilde{j}_{elec}(\omega) \end{pmatrix} = \begin{pmatrix} -\frac{1}{R_{exc}} - \frac{1}{R_{rec}} & \frac{R_s}{R_{exc}} \\ \frac{1}{R_{exc}} & -1 - \frac{R_s}{R_{exc}} \end{pmatrix}$$
$$\times \begin{pmatrix} \tilde{V}_{int}(\omega) \\ \tilde{j}_{elec}(\omega) \end{pmatrix} + \begin{pmatrix} \tilde{j}_\Phi(\omega) \\ 0 \end{pmatrix}. \tag{23}$$

In the case of IS, we have three variables that are evolving as a function of time: $\tilde{V}_{int}$, $\tilde{V}_{ext}$, and $\tilde{j}_{elec}$. We thus require an additional equation that creates a 3×3 matrix. We therefore consider an arbitrarily small geometric capacitor, C_b, that is placed before R_s, with current $\tilde{j}_{term}$ flowing at the terminals to yield the relationship $C_b(d\tilde{V}_{ext}/dt) = \tilde{j}_{elec} - \tilde{j}_{term}$ and give a 3×3 matrix as

$$i\omega \begin{pmatrix} C_\mu & 0 & 0 \\ 0 & C_g & C_g R_s \\ 0 & C_b & 0 \end{pmatrix} \begin{pmatrix} \tilde{V}_{int}(\omega) \\ \tilde{V}_{ext}(\omega) \\ \tilde{j}_{elec}(\omega) \end{pmatrix}$$
$$= \begin{pmatrix} -\frac{1}{R_{exc}} - \frac{1}{R_{rec}} & \frac{1}{R_{exc}} & \frac{R_s}{R_{exc}} \\ \frac{1}{R_{exc}} & -\frac{1}{R_{exc}} & -1 - \frac{R_s}{R_{exc}} \\ 0 & 0 & 1 \end{pmatrix} \begin{pmatrix} \tilde{V}_{int}(\omega) \\ \tilde{V}_{ext}(\omega) \\ \tilde{j}_{elec}(\omega) \end{pmatrix}$$
$$+ \begin{pmatrix} \tilde{j}_\Phi(\omega) \\ 0 \\ -\tilde{j}_{term}(\omega) \end{pmatrix}. \tag{24}$$

The matrices in Eqs. (22)–(24) are of the form $C\dot{X} = AX + B$, where X is the matrix that contains the variables that need to be solved ($\tilde{V}_{int}$, $\tilde{V}_{ext}$, and $\tilde{j}_{elec}$) and the overdot indicates a first differential in time (or $i\omega$ in the frequency domain). Thus, the full solution is obtained by solving for the eigenvalues and eigenvectors of the $C^{-1}A$ matrix. The $n \times n$ $C^{-1}A$ matrix yields eigenvalues $\lambda_1 \ldots \lambda_n$, which are connected to the time constants through $\lambda_n = -1/\tau_n$. The solutions of the matrices in Eqs. (22)–(24) and their corresponding solutions in the time domain are shown in Table S3 within the Supplemental Material [48]. While a simple analytical solution for the time constants of IS is not achievable, an analytical solution of the transfer function can be obtained using the relationship $Z = W/Q$ [10]. In the case of frequency domain measurements, the expressed time constants are determined from the peak of the imaginary part of the solution of the transfer function (Table S3 within the Supplemental Material [48]) versus frequency. In addition, we note that the matrices in Eqs. (22)–(24)

are applicable only under dc open-circuit conditions. The general matrices corresponding to any applied dc external voltage, V_{ext} (i.e., when $V_{\text{int}} \neq V_{\text{elec}}$), are shown in Sec. A3 within the Supplemental Material [48] (Eqs. S37–S42).

D. Equivalent circuit

An alternative way of solving for the time constants is to use Eqs. (20) and (21) to calculate the IMVS, IMPS, and IS transfer functions, followed by obtaining the expressed time constants from the frequency maxima of the negative imaginary part of the transfer function. These are the IMVS transfer function, W; the IMPS transfer function, Q; and the impedance transfer function, Z, given by (the derivation is given in Sec. A4 within the Supplemental Material [48])

$$W = \frac{\tilde{V}_{\text{ext}}}{\tilde{j}_{\Phi}} = \left(\frac{1}{R_{\text{rec}}} + i\omega C_{\mu} + i\omega C_{\text{g}} \left(1 + \frac{R_{\text{exc}}}{R_{\text{rec}}} + i\omega R_{\text{exc}} C_{\mu} \right) \right)^{-1}, \tag{25}$$

$$Q = \frac{\tilde{j}_{\text{elec}}}{\tilde{j}_{\Phi}} = \left(1 + \frac{R_{\text{s}} + R_{\text{exc}}}{R_{\text{rec}}} + i\omega (R_{\text{s}} + R_{\text{exc}}) C_{\mu} + i\omega R_{\text{s}} C_{\text{g}} \left(1 + \frac{R_{\text{exc}}}{R_{\text{rec}}} + i\omega R_{\text{exc}} C_{\mu} \right) \right)^{-1}, \tag{26}$$

$$Z = \frac{\tilde{V}_{\text{ext}}}{\tilde{j}_{\text{elec}}} = R_{\text{s}} + \left(\frac{1}{R_{\text{exc}} + ((1/R_{\text{rec}}) + i\omega C_{\mu})^{-1}} + i\omega C_{\text{g}} \right)^{-1} = \frac{W}{Q}. \tag{27}$$

Equations (25)–(27) yield the equivalent circuit of Fig. 2(b). This circuit contains the traditional elements of the solar cell model with the parallel combination of the recombination resistance and chemical capacitance [41]. The novel aspect of the model is the voltage-dependent exchange resistance, R_{exc} (which is in series with the $R_{\text{rec}} C_{\mu}$ line), which models the potential drop across the transport layers. Equations (4), (6), and (13) show that R_{exc} depends on the steady-state quasi-Fermi level splitting at the electrodes, V_{elec}, and the mobility and electric field through the transport layer. Equations (25) and (26) identify a time constant called the charge carrier exchange lifetime, as given by (valid only under open-circuit conditions)

$$\tau_{\text{exc}} = R_{\text{exc}} C_{\mu} = \frac{d}{S_{\text{exc}}}. \tag{28}$$

The exchange lifetime determines how quickly charge carriers are extracted from (injected into) the volume of the absorber into (from) the contacts through the transport layers. We note that resistance R_{exc} is defined only under small-perturbation conditions and is different from the steady-state transport layer resistance derived in our previous work [18]. The generation term is in the form of a current source, j_{Φ}, that is across the bulk $R_{\text{rec}} C_{\mu}$ line, corresponding to internal voltage V_{int}. The model is completed with geometric capacitance C_{g}, which is in parallel to all the elements that are outside the external series resistance, R_{s}. We clarify that capacitor C_{b} is ignored in the equivalent circuit because it is made arbitrarily small and, hence, has no influence on the solution of the model.

E. Model analysis

We now proceed to analyze the solution of the model at different open-circuit voltages. The parameters used to carry out the simulations are shown in Table S4 within the Supplemental Material [48] and discussed in Sec. A5 within the Supplemental Material [48], with a list of input and output parameters of the model shown in Fig. S4 within the Supplemental Material [48]. We consider two cases, one where the extraction lifetime is much faster than the effective recombination lifetime ($\tau_{\text{exc}} \ll \tau_{\text{eff}}$), which we refer to as "fast charge carrier extraction," and the other case where the extraction lifetime is much slower than the effective recombination lifetime ($\tau_{\text{exc}} \gg \tau_{\text{eff}}$), which we refer to as "slow charge carrier extraction." To simulate these two situations, the transport layer mobility is varied between 10^{-1} and 10^{-5} cm^2 V^{-1}s^{-1}. τ_{exc} is calculated by determining S_{exc} using Eq. (6) or, equivalently, by determining R_{exc} and C_{μ} using Eqs. (10) and (13) and using the relationship $V_{\text{int}} = V_{\text{elec}}$ under open-circuit conditions. Summaries of these solutions are shown in Figs. 3(a) and 3(b) for the case of fast charge carrier extraction, with the case of slow charge carrier extraction shown in the corresponding lower panels [Figs. 3(c) and 3(d)]. We note that the time constants for IS and IMVS are identical, and we therefore plot the IMVS time constants in Fig. S6 within the Supplemental Material [48] and show only the time constants of IS and IMPS in our analysis. In addition, the IS matrix yields a third time constant, which corresponds to $\tau = R_{\text{s}} C_{\text{b}}$, that attenuates the total current response. However, since C_{b} is a capacitor that is introduced only to facilitate solving the IS matrix, we consequently make C_{b} arbitrarily small and, hence, $\tau =$

R_sC_b is also arbitrarily small and can be neglected in our analysis.

In all cases, the model yields two time constants that correspond to each of the inverse eigenvalues, which are classified as slow (τ_{slow}) or fast (τ_{fast}) time constants with respect to each other. These eigenvalues are combined with their eigenvectors to yield the full solution of the transfer function (Table S3 within the Supplemental Material [48]). However, the traditional analysis method of frequency domain data involves calculating time constants from the frequency maxima of the negative imaginary part of the transfer function. We therefore calculate the full solution of the matrices using the eigenvalues and eigenvectors to obtain the analytical solution of the respective transfer function, the time constants of which are calculated from the frequency maxima of the negative imaginary part of the transfer function. An alternative way of calculating the time constants is to apply the same method to the equivalent circuit solution for the respective transfer function from Eqs. (25)–(27). Both the analytical solution (line labeled solution in Fig. 3) and the EC solution (line labeled EC in Fig. 3) yield only one time constant from the frequency maxima of the negative imaginary part of the transfer function, which corresponds to the slow time constant, τ_{slow} (see Fig. S5 within the Supplemental Material

[48] for Nyquist plots, as summarized in Fig. 4). Therefore, the fast time constant, τ_{fast}, is hidden from the traditional analysis of the negative imaginary part of the frequency domain transfer function. We developed a new analysis method in Ref. [42] that allowed the hidden time constant τ_{fast} to be extracted from the frequency domain data; however, its discussion is beyond the scope of this paper.

For the case of fast charge carrier extraction [$\tau_{exc} \ll \tau_{eff}$, Figs. 3(a) and 3(b)], the IS and IMPS solutions yield a slow time constant that corresponds to the effective recombination lifetime, τ_{eff}, under large open-circuit voltages. τ_{eff} is voltage dependent due to the dominance of radiative recombination over SRH recombination at high open-circuit voltages [Eq. (15)]. In the absence of radiative recombination, τ_{eff} will correspond to the constant SRH lifetime, which forms a plateau in the time constant. This region then transitions into an exponentially increasing time constant at lower open-circuit voltages. For IMPS, the slow time constant corresponds to the product of the series resistance, R_s, and the geometric capacitance, C_g, at lower open-circuit voltages (referred to as RC attenuation in the literature [43,44]) and transitions to τ_{eff} at higher open-circuit voltages. The fast time constant for all the transfer functions corresponds to the exchange lifetime, τ_{exc}, at lower open-circuit voltages before transitioning to
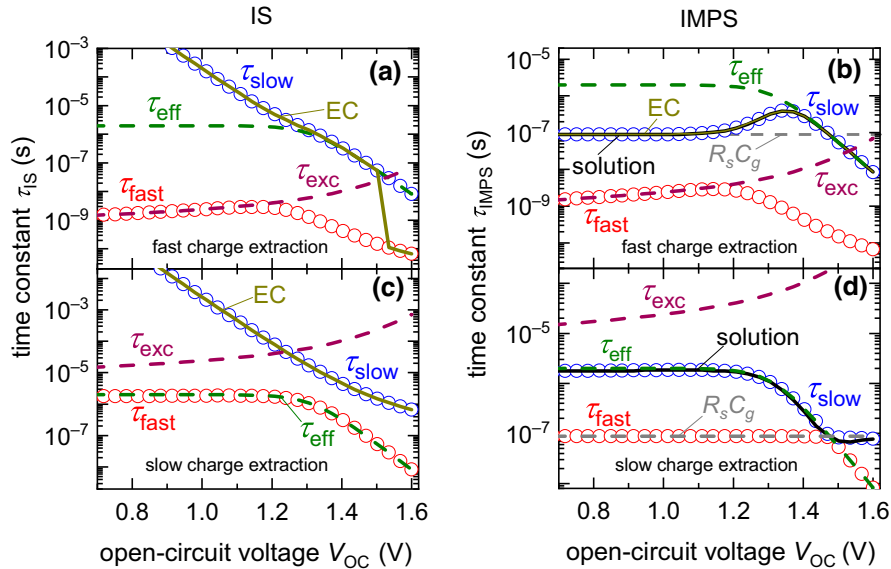

FIG. 3. Simulated analytical time constants τ_{slow} and τ_{fast} from the matrix model for $\tau_{exc} \ll \tau_{eff}$ (a),(b) and $\tau_{exc} \gg \tau_{eff}$ (c),(d), for IS (a),(c) and IMPS (b),(d). To simulate these two situations, transport layer mobility is varied between 10^{-1} and 10^{-5} cm^2 V^{-1} s^{-1}. Fast charge extraction corresponds to the case $\tau_{exc} \ll \tau_{eff}$, while slow charge extraction corresponds to the case $\tau_{exc} \gg \tau_{eff}$. IMVS time constants are identical to those of IS, as shown in Fig. S6 within the Supplemental Material [48]. "Solution" and "EC" correspond to the time constant calculated from the frequency maxima of the negative imaginary part of the analytical solution of the transfer function (see Table S3 within the Supplemental Material [48]) and the equivalent circuit, respectively. Expressed time constant from the analysis of the negative imaginary part of the transfer function is always the slower time constant, τ_{slow}. τ_{eff} is the effective recombination lifetime, consisting of the parallel combination of SRH and radiative recombination, and τ_{exc} is the exchange lifetime between the perovskite absorber and contacts [Eq. (28)]. Simulation parameters are shown in Table S4 within the Supplemental Material [48]. Equality of the EC solution and analytical solution of IS are shown in Fig. S7 within the Supplemental Material [48].
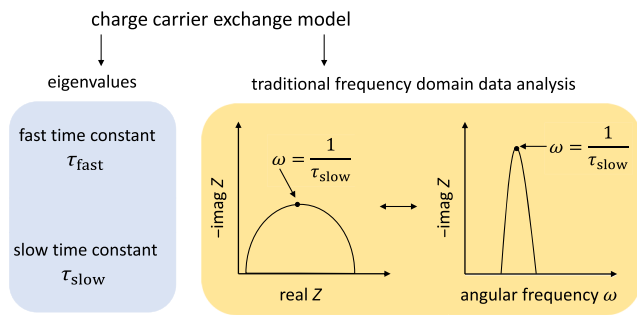
FIG. 4. Schematic of the methods used to obtain time constants using our developed model. While the analytical solution of the model predicts the existence of two eigenvalues that correspond to two time constants, τ_{fast} and τ_{slow}, traditional analysis of the negative imaginary part of the simulated frequency domain transfer function yields only τ_{slow}. Therefore, τ_{fast} cannot be obtained using this method and requires a modification of the transfer function to be extracted from the data, as described in Ref. [42].

an exponential reduction at higher open-circuit voltages. The open-circuit voltage dependence of τ_{exc} arises from Eqs. (5) and (6) with $V_{\text{elec}} = V_{\text{oc}}$, causing it to increase at higher open-circuit voltages.

For the case of slow charge carrier extraction [$\tau_{\text{exc}} \gg \tau_{\text{eff}}$, Figs. 3(c) and 3(d)], in the case of IS, the fast time constant corresponds to τ_{eff}. The slow time constant does not follow τ_{exc} but shows a much larger magnitude at low open-circuit voltages, decreasing exponentially, followed by saturation at high open-circuit voltages. In the case of IMPS, the fast time constant corresponds to the $R_s C_g$ product, while the slow time constant corresponds to τ_{eff}. At large open-circuit voltages, the IMPS fast and slow time constants are exchanged, which results in the time constant values not crossing each other. We highlight that, for all the transfer functions, in both cases, the time constant obtained

from the frequency maxima of the negative imaginary part of the transfer function (calculated from both the solution of the model and the equivalent circuit) corresponds to the slower time constant. Therefore, when $\tau_{\text{exc}} \ll \tau_{\text{eff}}$, which is the case expected for a high-efficiency PSC with efficient charge carrier extraction from the perovskite to the contacts through the transport layers, the faster time constant that contains information on the exchange properties is not directly accessible using the traditional data analysis method.

We now aim to identify the different unknown contributions to the slow and fast time constants, as shown in Fig. 5. For the case of fast charge carrier extraction, the exponential drop in the fast time constant at high open-circuit voltages for all the transfer functions is determined by the product $R_{\text{exc}} C_g$. We note that, in Fig. 3(a), there is an abrupt transition of the time constant seen in the Nyquist plot (labeled EC) from τ_{slow} to τ_{fast} at high open-circuit voltage, because the dominant time constant in the EC changes depending on whether the effective recombination time constant or the charge carrier exchange time constant is faster [equivalent to the transition from Figs. 6(a) to 6(c)]. Furthermore, the exponential rise in the slow (expressed) time constant for IS [Fig. 5(a)] at low open-circuit voltages corresponds to the product of the recombination resistance, R_{rec}, and the geometric capacitance, C_g. This coupling can also be seen from the experimental resistances and capacitances [Figs. 1(b) and 1(c), respectively] at low open-circuit voltages, where the resistance increases exponentially, while the capacitance has saturated to a constant value. This effect was labeled as the recombination of electrode charges by Kiermasch *et al.* [8], who identified this effect for different photovoltaic technologies when observing large lifetimes in the order of milliseconds to seconds from TPV and open-circuit voltage decay measurements. The same
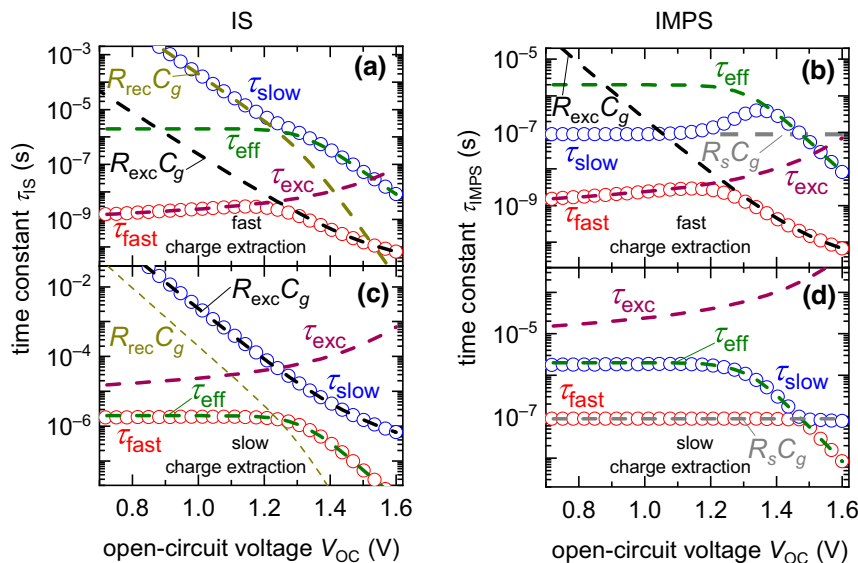

FIG. 5. Simulated analytical time constants τ_{slow} and τ_{fast} from the model (same as in Fig. 3), with different contributions to the time constants shown with the corresponding labels. Fast charge extraction corresponds to the case of $\tau_{\text{exc}} \ll \tau_{\text{eff}}$, while slow charge extraction corresponds to the case of $\tau_{\text{exc}} \gg \tau_{\text{eff}}$. R_{rec} is the recombination resistance [Eq. (15)], while R_{exc} is the exchange resistance [Eq. (13)]. For IS measurements, $R_{\text{rec}} C_g$ dominates the expressed time constant (τ_{slow}) at lower open-circuit voltages when $\tau_{\text{exc}} \ll \tau_{\text{eff}}$, while $R_{\text{exc}} C_g$ dominates the expressed time constant when $\tau_{\text{exc}} \gg \tau_{\text{eff}}$. τ_{fast} for IS is given by τ_{exc} at low open-circuit voltages followed by $R_{\text{exc}} C_g$ at high open-circuit voltages when $\tau_{\text{exc}} \ll \tau_{\text{eff}}$, while $\tau_{\text{fast}} = \tau_{\text{eff}}$ for the case of $\tau_{\text{exc}} \gg \tau_{\text{eff}}$.

phenomenon was later reported on by Wang *et al.* [28] in the case of TPV measurements and IS simulations, who concluded that the lifetimes observed were not representative of recombination dynamics but dominated by the geometric capacitance of the device. Krückemeier *et al.* [7] also compared the reported lifetimes from TPV and TRPL measurements, concluding that the much larger lifetimes reported from TPV measurements were due to measurement of this $R_{rec}C_g$ time constant. This occurs because TPV measurements require a full device with electrodes that introduces the effects of the geometric capacitance, whereas TRPL is mostly measured on device stacks without electrodes. We note that the exponential rise of this slow time constant at low open-circuit voltages is limited by the voltage-independent shunt resistance of the perovskite layer [45].

For the case of slow charge carrier extraction, the slow time constant in the case of IS is determined by the product of R_{exc} and C_g. The voltage dependence of the extraction velocity, S_{exc} [Eq. (6)], creates a unique evolution of R_{exc} [Eq. (13)] and, hence, the $R_{exc}C_g$ time constant, which shows an exponential decrease followed by a saturation at high open-circuit voltages; this could be misinterpreted as an apparent SRH lifetime. Since the slow time constant is the one that is expressed during a measurement, information regarding the transport layer can be obtained through the determination of R_{exc} as a function of the open-circuit voltage in this case. An intermediate case is shown in Fig. S8 within the Supplemental Material [48] for IS measurements, when $\tau_{exc} \cong \tau_{eff}$. In this case, the resistance at large open-circuit voltages is dominated by R_{exc}, while, at lower open-circuit voltages, R_{rec} dominates. This situation leads to the slow (expressed) time constant at large open-circuit voltages being dominated by the $R_{exc}C_g$ product, which makes a plateau, while, at lower open-circuit voltages, it is dominated by the product $R_{rec}C_g$.

In summary, the model predicts that two time constants are expressed under different dc conditions in frequency domain small-perturbation measurements. These are a slow and fast time constant (compared to each other), which correspond to different RC products that arise from coupling between physical mechanisms, such as charge carrier recombination, injection, and extraction. From the traditional analysis of frequency domain data, only the slow time constant can be extracted, while the fast time constant remains hidden below the arc of the slow time constant. In the case of fast charge carrier extraction compared to recombination, this slow time constant corresponds to bulk recombination at high open-circuit voltages and recombination limited by the back-injection of electrode charges at low open-circuit voltages. For the case of slow charge carrier extraction compared to recombination, the slow time constant is controlled by the resistance of the transport layer. Therefore, irrespective of the magnitudes of the measured time constants, only in situations where the transport layer mobility is large enough to ensure fast charge carrier extraction (i.e., $\tau_{exc} \ll \tau_{eff}$) can the measured time constants at high open-circuit voltages be considered a real recombination lifetime.

To provide an intuitive connection between the equivalent circuit and the measured time constants, we calculate the reduced equivalent circuits for each case and compare them to the obtained time constants from the model, as shown in Fig. 6. For the case of fast charge extraction ($\tau_{exc} \ll \tau_{eff}$), there are two possible scenarios. At a large forward bias, when the chemical capacitance is much larger than the geometric capacitance and the effective resistance, R_{eff}, is simply a series connection of series resistance R_s, exchange resistance R_{exc}, and recombination resistance R_{rec}, the time constant is given by the bulk recombination lifetime, $\tau_{eff} = R_{rec}C_\mu$ [Fig. 6(a)]. At reverse and low forward bias, the chemical capacitance
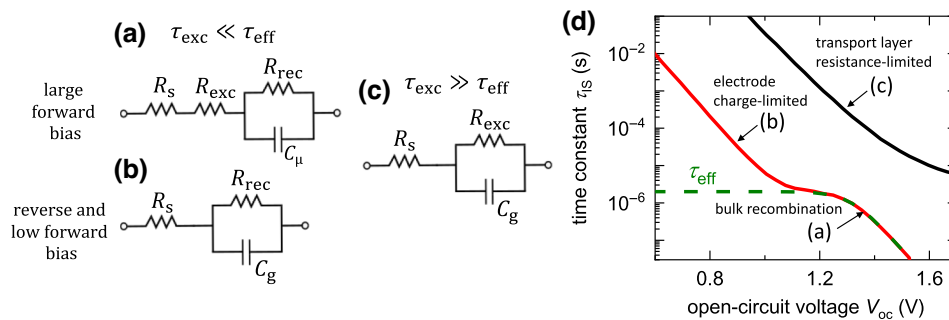

FIG. 6. Reduced equivalent circuit derived from the matrix model [see Fig. 2(b)] for the special cases (a),(b) $\tau_{exc} \ll \tau_{eff}$ and (c) $\tau_{exc} \gg \tau_{eff}$. (a) Case where chemical capacitance C_μ is much larger than geometric capacitance C_g (large forward bias), while (b) corresponds to $C_\mu \ll C_g$ (reverse bias and low forward bias). (d) $R||C$ products that form the time constant in each case [$\tau = \tau_{eff} = R_{rec}C_\mu$ in (a), $\tau = R_{rec}C_g$ in (b), and $\tau = R_{exc}C_g$ in (c)] are the expressed time constants in an IS measurement. Total resistance of the PSC is determined by the sum of series resistance R_s, exchange resistance R_{exc}, and recombination resistance R_{rec} (i.e., they are in series).

is smaller than the geometric capacitance and the effective resistance is dominated by the series resistance and the recombination resistance, while the time constant is given by $\tau = R_{rec}C_g$ [Fig. 6(b)]. In such situations of fast charge carrier extraction, the measured time constant can be considered as the product of the differential resistance and effective capacitance (geometric capacitance at low forward bias and chemical capacitance at large forward bias) of the device [45]. For the case of slow charge extraction ($\tau_{exc} \gg \tau_{eff}$), the total resistance is a series connection of R_s and R_{exc}, with the time constant given by $\tau = R_{exc}C_g$ [Fig. 6(c)]. The effective capacitance, C_{eff}, in all cases, depends not only on the individual capacitances but also on the resistances (Eqs. S70 and S73 in Sec. A6 within the Supplemental Material) [18,48]. This effect is seen in Fig. S9 within the Supplemental Material [48], where both the series resistance and exchange resistance create a saturation of the effective capacitance calculated from the model (also discussed in Ref. [46]).

These time constants are also shown as a function of open-circuit voltage in Fig. 6(d). As discussed previously, in the case of slow charge extraction ($\tau_{exc} \gg \tau_{eff}$), the measured time constants from IS are dominated by the resistance of the transport layer. When the mobility of the transport layer is high enough to ensure efficient charge extraction ($\tau_{exc} \ll \tau_{eff}$), the time constants are controlled by bulk recombination at large open-circuit voltages while being limited by charges back-injected from the electrodes at lower open-circuit voltages.

Based on the predictions of the model in Secs. III D and III E, we suggest that the best method to characterize the PSC is a combination of any two of the three frequency domain methods. This is because of the relationship between the transfer functions, $Z = W/Q$, which is proven experimentally for the PSC [10], and implies that all the information of the system can be obtained from the measurement of any two of the three transfer functions. We further encourage the measurement of these spectra and calculated parameters over a wide range of dc conditions, such as light intensity, external voltage, and current density, to discriminate between different physical mechanisms based on their characteristic evolution versus dc parameters.

IV. SIMULATIONS

To confirm the validity of our model, we carry out IS simulations on a *p-i-n* PSC with the structure ITO/PTAA/perovskite/PCBM/Ag, the band diagram of which is shown in Fig. 7(a). For simplicity, we consider no band offsets between the perovskite and transport layers, mobilities of electrons and holes to be equal in the respective layers, and no external series resistance ($R_s = 0$). We consider a uniform volume density of mid-gap electron

(acceptorlike) traps, N_t, through the perovskite layer. Further details of the simulation parameters are shown in Table S5 within the Supplemental Material [48]. We also neglect ionic densities within the perovskite layer, since we are interested only in electronic phenomena and because the ionic contributions to the PSC spectra are known to occur below about 10^3 Hz in IS measurements [24], indicating that the response at frequencies above this value are purely electronic in nature and, hence, can be represented by a purely electronic model. The strategy of this section is to simulate situations of increasing complexity, starting from equal mobilities of the perovskite and transport layers up to the situation of a full device with varying mobilities of the transport layers, to identify if the influence of bulk recombination can be separated from transport-layer-related effects in the frequency domain response of the PSC.

A. Perfectly conducting transport layers with no bulk electric field

We begin by considering equal mobilities of the perovskite layer ($\mu_{pero} = 20$ cm^2/Vs) and the transport layers. We further make the relative permittivity of the perovskite very high ($\varepsilon_{r,pero} = 3 \times 10^5$) to ensure that there is no electric field in the perovskite layer. Figure 7(b) shows the time constants calculated from the maxima of the imaginary part of the simulated IS transfer function for different SRH lifetimes. These time constants decrease exponentially with increasing open-circuit voltage, with a subsequent change in slope that leads to approaching the same value ($\sim 10^{-7}$ s) at high open-circuit voltages. For the same open-circuit voltage, a larger SRH lifetime corresponds to a larger magnitude of the time constant. Figures 7(c) and 7(d) show the resistance and capacitance, respectively, the product of which yields the measured time constants.

We define a factor m that controls the slope of the exponential evolution of resistances R and capacitances C (which correspond to the effective resistance, R_{eff}, and effective capacitance, C_{eff}, as defined in Sec. III E and in Sec. A6 within the Supplemental Material [48]) with respect to the open-circuit voltage, given by

$$R \propto \exp\left(-\frac{qV_{OC}}{m_R k_B T}\right), \qquad (29)$$

$$C \propto \exp\left(\frac{qV_{OC}}{m_C k_B T}\right). \qquad (30)$$

The slope factors of the resistances and capacitances in Fig. 7 are shown in Fig. S10 within the Supplemental Material [48]. The capacitance evolves identically for all cases, transitioning from the geometric capacitance
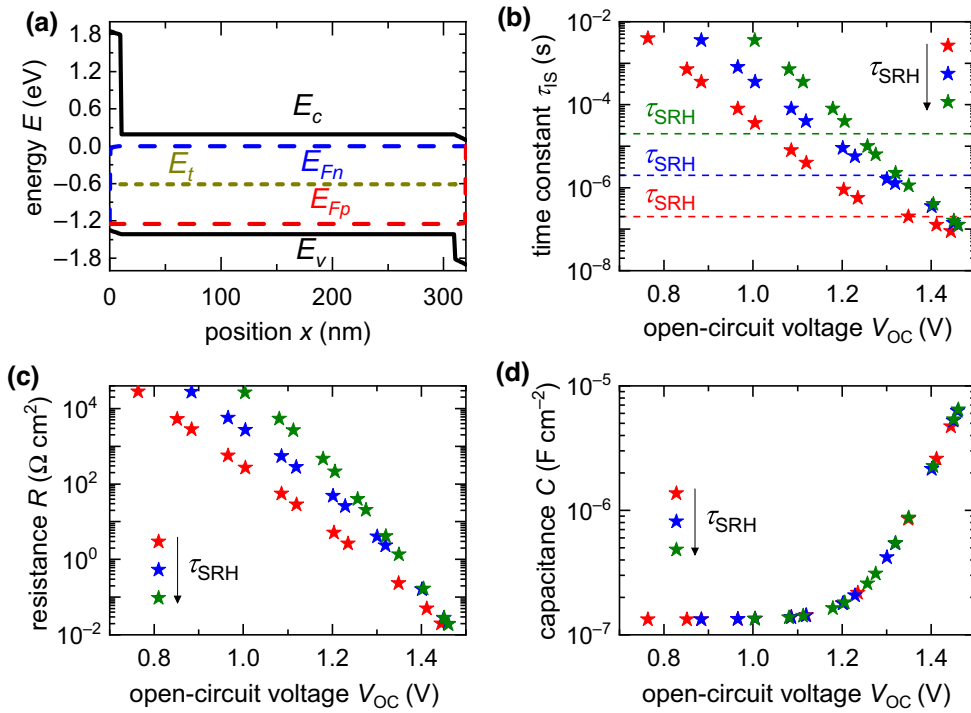
FIG. 7. (a) Band diagram of the ITO/PTAA/perovskite/PCBM/Ag PSC upon which the drift-diffusion simulations are based. Relative permittivity of the perovskite is increased arbitrarily high to ensure no electric field within the perovskite layer. Mobilities of the transport layers are made equal to that of the perovskite layer. Calculated (a) high-frequency time constants and corresponding (b) resistances and (c) capacitances from IS simulations at open circuit for different SRH lifetimes [dotted lines in (b)]. Simulation parameters are shown in Table S5 within the Supplemental Material [48]. Radiative recombination prevents the observation of the plateau in the time constant corresponding to SRH recombination.

at low open-circuit voltages to an exponential increase with a slope factor, m_C, that approaches a value of two at high open-circuit voltages, corresponding to the chemical capacitance of an intrinsic layer [Eq. (10)]. The resistances show a slope factor, m_R, equal to two at low open-circuit voltages, corresponding to the dominance of first-order SRH recombination in the bulk [Eq. (15)]. For higher open-circuit voltages, m_R transitions to a value of one, corresponding to the dominance of second-order radiative recombination. Therefore, the product of the resistances and capacitances in the low open-circuit voltage regime shows an exponential evolution ($\tau = R_{\text{rec,SRH}} C_g \propto \exp(-qV_{\text{OC}}/2k_BT)$), while, in the high open-circuit voltage regime, the exponential trend is maintained due to their differing slopes ($\tau = \tau_{\text{rad}} \propto \exp(-qV_{\text{OC}}/2k_BT)$), leading to the time constants not saturating anywhere near their respective SRH lifetimes. An exception is the case of the smallest SRH lifetime [red stars in Fig. 7(b)] due to its slower transition of m_R from a value of two compared to the other two cases. We thus speculate that the onset of radiative recombination prevents the observation of a plateau that corresponds to the SRH lifetime; this is also observed in the simulations from the matrix model shown in Fig. 3(a).

B. Perfectly conducting transport layers with no bulk electric field and no radiative recombination

To confirm our hypothesis, we switch off radiative recombination and redo the simulations of the previous section, as shown in Fig. 8. We find that the time constants (symbols) now saturate nicely at the respective SRH

lifetime under high open-circuit voltages. The slope factors of the resistances and capacitances are shown in Fig. S11 within the Supplemental Material [48]. The capacitances [symbols in Fig. 8(c)] again evolve identically in all cases, with a slope factor of about two at high open-circuit voltages corresponding to the chemical capacitance, C_μ, and the geometric capacitance, C_g, expressed at low open-circuit voltages. The resistances [symbols in Fig. 8(b)] also show a slope factor close to two, indicating a first-order SRH recombination resistance through the entire voltage range. Therefore, at low open-circuit voltages, we again observe the exponential C_g-dominated lifetime. At high open-circuit voltages, when the capacitance transitions from C_g to C_μ, the product of the SRH recombination resistance and C_μ yields the constant SRH lifetime. Furthermore, the predicted time constants, resistances, and capacitances from the model [lines in Figs. 8(a)–8(c)] match nicely with simulated data. The predicted saturation of the capacitance at low voltages, C_{sat}, from the model is different from that of the simulations because C_g of the transport layers is not included in the model ($C_{\text{sat}} = [1/C_{g,\text{ETL}} + 1/C_{g,\text{pero}} + 1/C_{g,\text{HTL}}]^{-1}$) [18].

C. Perfectly conducting HTL with variable ETL mobility

We now increase the complexity of the simulations further by varying the mobility of the ETL while keeping the HTL mobility equal to that of the perovskite layer. The simulated time constants are shown in Fig. 9(a), with the corresponding resistances and capacitances shown in Figs. 9(b) and 9(c), respectively. Quantities corresponding
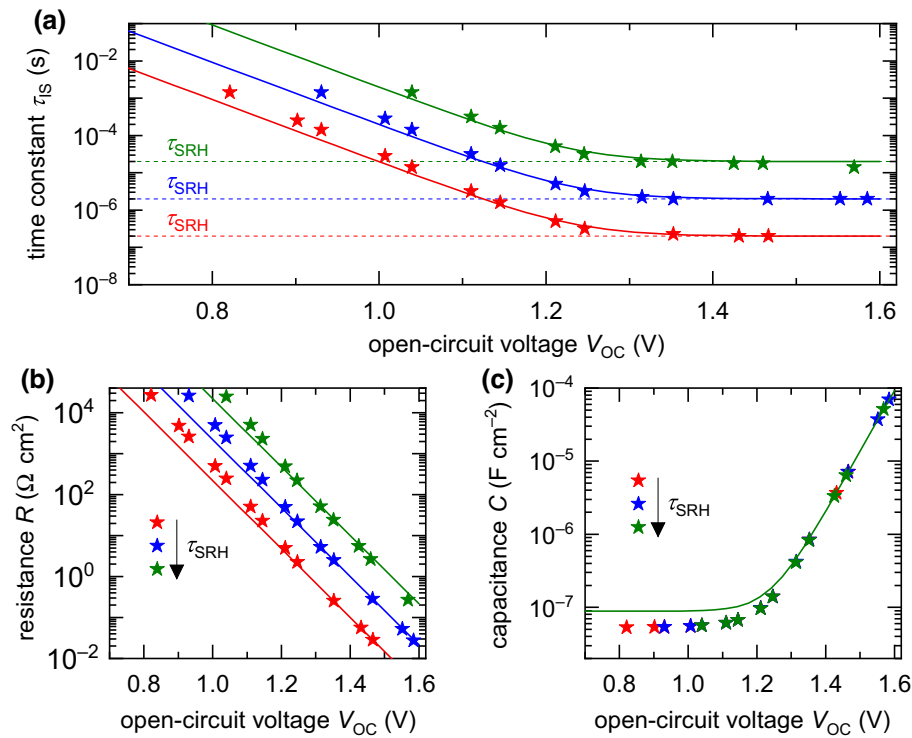
FIG. 8.   Calculated (symbols) (a) high-frequency time constants and corresponding (b) resistances and (c) capacitances from IS simulations at open circuit for different SRH lifetimes [dotted lines in (a)] from drift-diffusion simulations of the PSC. In addition to ensuring no electric field in the perovskite layer with an arbitrarily high relative permittivity, radiative recombination is switched off for the perovskite layer. Mobilities of the transport layers are set equal to that of the perovskite layer. Simulation parameters are shown in Table S5 within the Supplemental Material [48]. Lines in (a)–(c) are the corresponding predictions from the model. Absence of radiative recombination allows the observation of a plateau in the time constant, which corresponds to the SRH lifetime. Saturation of the capacitance at low open-circuit voltages predicted by the matrix model is different from the simulations because the model does not consider the individual geometric capacitances of the transport layers.

to different mobilities of the ETL are represented using both symbols, as shown in the legend, and varying line darkness, while different SRH lifetimes are represented using different colors. The time constants show the same exponential evolution at low open-circuit voltages due to the dominance of C_g, as discussed in previous cases (Figs. 7 and 8), irrespective of the ETL mobility. At higher open-circuit voltages, this transitions into a plateau that shows a weak evolution versus open-circuit voltage and is strongly dependent on the ETL mobility but independent of the SRH lifetime. For lower mobilities, the time constant saturates at a corresponding larger value. Therefore, we conclude that the plateau region is not a real SRH lifetime in this case.

The corresponding resistances in Fig. 9(b) show two regimes, the first being an exponential evolution at low open-circuit voltages, followed by a transition to a plateau at high open-circuit voltages, similar to the time constants. For higher mobilities of the ETL, we expect that, based on the findings of the previous sections, the exponential evolution at low open-circuit voltages is dominated by SRH recombination ($m_R = 2$). At higher open-circuit

voltages, this region should transition into a steeper exponential drop due to the dominance of radiative recombination ($m_R = 1$). However, for lower ETL mobilities, the resistance makes a plateau at high open-circuit voltages. Simulations of the evolution of the total resistance versus transport layer mobility and open-circuit voltage from the model (Fig. S12 in the Supplemental Material [48]) show the same trends as those observed in Fig. 9(b), where the larger resistance between R_{exc} and R_{rec} dominates the measured resistance (i.e., R_{exc} and R_{rec} are in series, as shown in Fig. 6). Therefore, for lower mobilities of the ETL, the expressed resistance is indeed R_{exc}, which transitions into the R_{rec}-dominated resistance for high ETL mobilities. The transition from R_{rec} to R_{exc} for reducing mobilities of the ETL is difficult to identify, since both resistances possess the same slope factor of $m_R = 2$ [see Eqs. (13) and (15)] at low open-circuit voltages. The capacitance in Fig. 9(c) shows the typical geometric capacitance to chemical capacitance transition for high mobilities of the ETL. This transition is strongly dampened for lower ETL mobilities (larger R_{exc}), causing the capacitance to saturate at higher open-circuit voltages. This effect
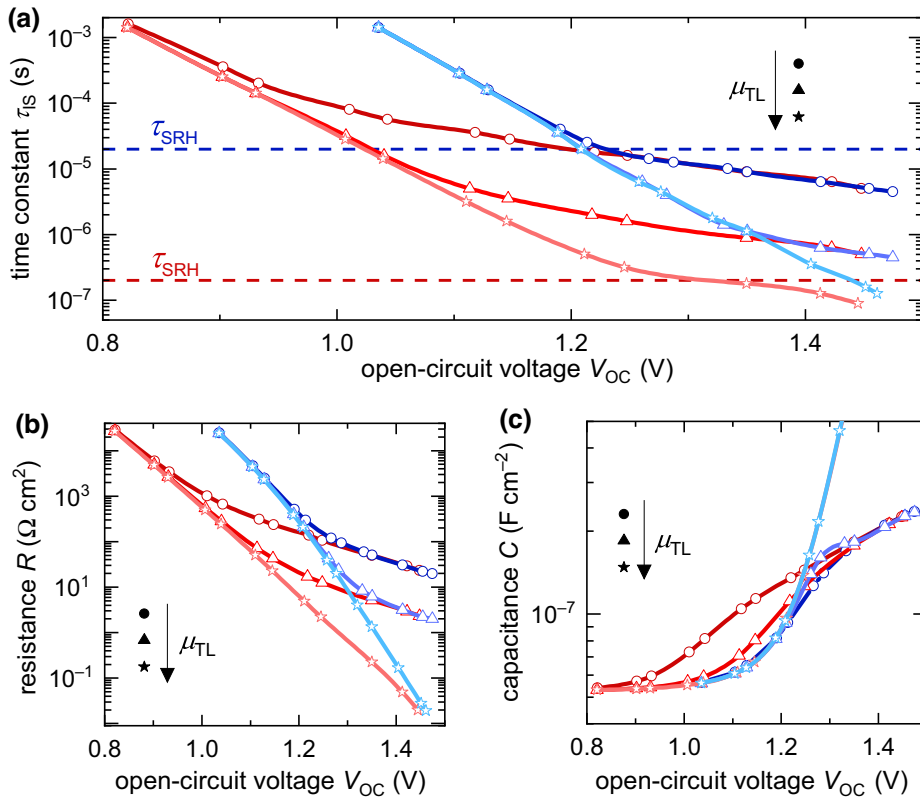
FIG. 9. Calculated (a) high-frequency time constants and corresponding (b) resistances and (c) capacitances from IS simulations at open circuit for different SRH lifetimes [dashed blue and red lines in (a)] from drift-diffusion simulations of a PSC, where the HTL mobility is set equal to the perovskite layer, while the ETL mobility is varied, as shown in the legend (stars correspond to the ETL mobility being equal to that of the perovskite layer). Reduced darkness of blue and red lines also corresponds to increasing mobility of the ETL layer for the respective SRH lifetime. Simulation parameters are shown in Table S5 within the Supplemental Material [48]. Exchange resistance, R_{exc}, dominates the resistance and time constant at high open-circuit voltages for lower mobilities of the ETL. Mobility range used for the ETL is $10^{-5} - 10^{-3}$ cm^2 V^{-1} s^{-1}.

of R_{exc} on the effective capacitance is also predicted by the model, as shown in Fig. S9 within the Supplemental Material [48].

To confirm the validity of our interpretation, we switch off radiative recombination and repeat the simulations; these results are shown in Fig. S13 within the Supplemental Material [48]. For the case of highest mobility of the ETL ($\mu_{ETL} = \mu_{pero}$, represented using stars), the time constants saturate at their respective SRH lifetimes, while also observing exponential R_{rec} through the entire range of open-circuit voltage and the chemical capacitance at large open-circuit voltages. For lower mobilities of the ETL, the SRH lifetimes are not expressed anymore but are instead replaced by the plateaus that are a function of the ETL mobility, with the corresponding dominance of R_{exc} observed in the resistances. In summary, we conclude that, for low mobilities of the transport layer, the plateaus in the time constants are not representative of the SRH lifetimes but are a consequence of the exchange resistance, R_{exc}. Therefore, analysis of the evolution of the high-frequency resistance versus dc open-circuit voltage is an effective tool to discriminate between the dominance of either bulk recombination or transport-layer-related effects in the frequency domain response of the PSC.

D. Variable ETL and HTL mobilities

We finally simulate the scenario of variable mobilities of both the ETL and HTL, as shown in Fig. S14 within

the Supplemental Material [48]. The time constants, resistances, and capacitances show an identical evolution as a function of mobility and open-circuit voltage to the case of a single transport layer with variable mobility (Fig. 9). We conclude that the salient features of the IS response of a full PSC with variable mobilities of the ETL and HTL is captured well by the model. However, the contribution of each transport layer to the observed resistance cannot be known from such an analysis, since our model assumes a symmetric PSC. Therefore, measurements on PSCs with the same ETL but different HTLs or vice versa will allow discriminating between the response of either transport layer.

V. DISCUSSION

Having established the validity of the model in Sec. IV, we now proceed to interpret the experimental IS data in Fig. 1. We note that the 1-sun open-circuit condition is chosen for the measurements because it implies flat Fermi levels under dc conditions; this allows the direct calculation of the magnitudes of the chemical capacitance and recombination resistance, which depend on the internal voltage, using $V_{int} = V_{elec}$. Second, it also leads to a small or completely absent electric field in the bulk of the perovskite layer, which is one of the assumptions of the model. We first analyze the three data points that do not show a plateau in the time constant: three SAM-C$_{60}$/BCP devices (samples 6, 7, and 8 in Fig. 1). The corresponding

slope factors of the resistances and capacitances are shown in Fig. S15 within the Supplemental Material [48]. The slope factor of the resistance shows a value between 1 and 2 at lower open-circuit voltages that transitions to lower values between 0.2 and 1 at higher open-circuit voltages. This behavior is similar to the transition between first-order to second-order recombination in Fig. 7(c), although it is unclear why the values go below one. The slope factor of the capacitance also decreases continuously from values above two to values below one, similar to a transition from the geometric capacitance to the chemical capacitance at high open-circuit voltages. We conclude that the recombination resistance, R_{rec}, dominates the measured resistances for devices with the SAM-C_{60}/BCP combination of transport layers, which therefore does not contain any information regarding the transport layer properties.

The dominance of R_{rec} in unison with the absence of a plateau region raises the following question: *under which conditions can the plateau region corresponding to the SRH lifetime be clearly observed?* We therefore calculate the width, ΔV_{sat}, of the plateau region to identify the parameters that it depends on. From the model, for $\tau_{exc} \ll \tau_{eff}$ [Fig. 5(a)], we know that ΔV_{sat} is determined by the intercept of the time constant $R_{rec}C_g$ with τ_{SRH} on the left side and τ_{rad} with τ_{SRH} on the right side, leading to (see Sec. A7 within the Supplemental Material [48] for the derivation)

$$\Delta V_{sat} = \frac{k_B T}{q} \ln \left(\frac{C_{\mu,0}}{C_g} \frac{\tau_{rad,0}}{\tau_{SRH}} \right), \qquad (31)$$

where $C_{\mu,0}$ and $\tau_{rad,0}$ are the equilibrium chemical capacitance and radiative lifetime, respectively. Equation (31) implies that $\Delta V_{sat} \propto \ln(d^2)$, which means ΔV_{sat} can be increased by increasing the thickness of the perovskite layer (thereby reducing the geometric capacitance). This effect is confirmed in the simulations corresponding to a thin and thick perovskite layer, as shown in Fig. 10, where the device corresponding to a thick perovskite layer shows an S-shaped evolution of the time constant with a clear plateau at τ_{SRH}, for large enough mobilities of the transport layer. Thus, moving from thin film devices to devices with a thick perovskite layer (lateral devices or single crystals) opens up an interesting possibility to clearly observe the SRH lifetime. The maximum thickness of the perovskite layer that can be used for this method is limited by the diffusion length of electrons and holes in the perovskite layer, to satisfy the model's assumption of a uniform charge carrier concentration in the perovskite layer. Considering a diffusion coefficient of $D = 1$ cm^2 s^{-1} [37,38] and a SRH lifetime of $\tau_{SRH} \cong 10^{-6}$ s (from the TRPL data in Fig. 1), we obtain a diffusion length of $L_D = \sqrt{D\tau_{SRH}} \cong 10$ μm, which implies that perovskite layer thicknesses up to 10 μm can be used to detect the SRH lifetime using our model.

We now analyze the data points that show a plateau in the time constant in Fig. 1. These correspond to samples 1–5, which include the PTAA-PCBM/BCP, PTAA-PCBM:CMC:ICBA/BCP, and PTAA-C_{60}/BCP combinations of transport layers. The corresponding slope factors of the resistances and capacitances are shown in Fig. S15 within the Supplemental Material [48]. The PTAA-PCBM/BCP devices (samples 1 and 2) show a transition of the resistance slope factor from a value about two at low open-circuit voltages to much larger values that correspond to a saturation of the resistance at large open-circuit voltages. This behavior is identical to the evolution of R_{exc}, as shown in Fig. 9(b) and Fig. S12 within the Supplemental Material [48]. If the plateau region in the time constant indeed corresponds to a real SRH lifetime, then the corresponding resistance would show an exponential trend throughout the entire range of open-circuit voltage, without any plateau, as shown in Fig. 8(b). A similar trend is observed for the resistance slope factors of samples 3–5, corresponding to the PTAA-PCBM:CMC:ICBA/BCP and PTAA-C_{60}/BCP combination of transport layers. However, for the case of $\tau_{exc} \cong \tau_{eff}$ shown in Fig. S8 within the Supplemental Material [48], we observe that, while R_{exc} dominates the plateau region of the time constants at large open-circuit voltages, R_{rec} dominates the exponential rise in the time constant at lower open-circuit voltages. Since we have no information regarding the value of τ_{SRH}, we conclude that the measured resistance at high frequencies for samples 1–5 are dominated by the exchange resistance, R_{exc}, only in the plateau region at large open-circuit voltages. This allows calculation of the exchange velocity, S_{exc}, using Eqs. (13) and (4), by

$$S_{exc} = \frac{2k_B T}{q^2 n_{int} R_{exc}} \exp \left(-\frac{q V_{OC}}{2 k_B T} \right). \qquad (32)$$

Since samples 1–5 all correspond to the same HTL, we speculate that the observed R_{exc} values originate from the PTAA layer. From the band gaps of the perovskite layers for samples 1–5 (Table S1 within the Supplemental Material [48]), we calculate (assuming a valence band density of states of $N_v = 10^{18}$ cm^{-3}) an intrinsic concentration of $n_i = p_i \cong 4.3 \times 10^4$ cm^{-3} for the perovskite layer in samples 1, 2, 4, and 5 and $n_i = p_i \cong 4 \times 10^3$ cm^{-3} in sample 3. We further assume a conduction band offset, Φ_b, of 0.08 eV at the perovskite-PTAA interface [47], which allows the interface concentration of holes to be calculated as $p_{int} = p_i \exp(q\Phi_b/k_B T) \cong 9.4 \times 10^5$ cm^{-3} for samples 1, 2, 4, and 5 and $p_{int} \cong 9.4 \times 10^4$ cm^{-3} for sample 3. The exchange lifetime, τ_{exc}, is then calculated using Eq. (28), assuming a thickness of $d = 300$ nm for the perovskite layer. If the electric field, F_{TL}, in the transport layers is known, we can then also estimate the mobilities in the transport layers from S_{exc} using Eq. (6). However, the electric field itself is very difficult to measure and estimates of
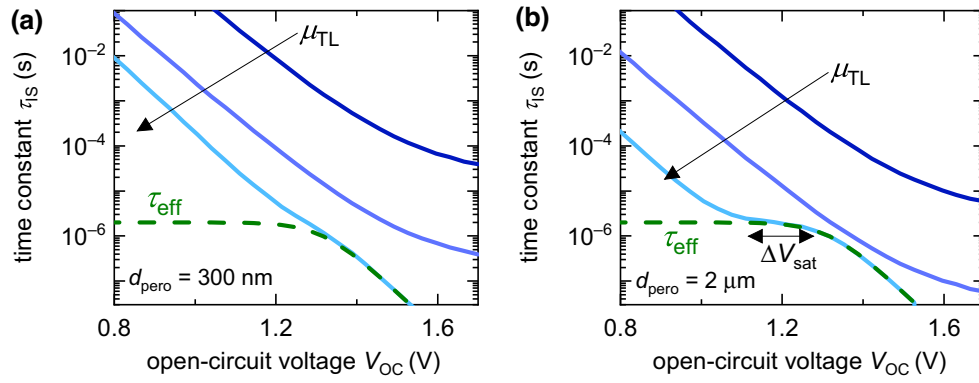
FIG. 10. Simulated time constants from the model for different mobilities, μ_{TL}, of the transport layer for (a) a thin perovskite layer of thickness 300 nm and (b) a thick perovskite layer of thickness 2 μm. For lower mobilities of the transport layer, time constants are dominated by transport layer resistance R_{exc}, while, for higher mobilities, the bulk recombination lifetime is expressed. Width of the plateau of the time constant that saturates at SRH lifetime τ_{SRH} is increased for the device with a thick perovskite layer [Eq. (31)]. Simulation parameters are shown in Table S4 within the Supplemental Material [48]. μ_{TL} is varied between 10^{-5} and 10 cm^2 V^{-1} s^{-1}.

the built-in electrostatic potential difference are generally quite crude in situations where the Mott-Schottky analysis fails (as is the case for perovskites) [18]. We assume that the built-in electrostatic potential difference in the transport layers, $V_{BI,TL}$, is comparable to the best open-circuit voltage values obtained for this band gap, since charge collection losses are maximized when the applied voltage is larger than the built-in electrostatic voltage [35]. Based on the 1-sun open-circuit voltage values and band gaps for samples 1–5 in Table S1 within the Supplemental Material [48], we thus assume that $V_{BI,TL}$ of samples 1–3 is approximated by the respective open-circuit voltages. Therefore, for samples 1–3 at 1-sun open-circuit voltage conditions, we assume a negligible electric field in the transport layers, which allows us to approximate the exponential in Eq. (6) with a first-order Taylor expansion, yielding

$$S_{exc}(V_{OC}(1 \text{ sun})) \cong \frac{\mu_{TL} F_{TL}}{1 - \left(1 - \frac{q F_{TL} d_{TL}}{k_B T}\right)} = \left(\frac{k_B T}{q}\right) \frac{\mu_{TL}}{d_{TL}}.$$

(33)

Equation (33) thus allows us to calculate the mobility of the transport layer from the S_{exc} value measured at 1-sun open-circuit voltage only for samples 1–3. Figure 11 shows the calculated S_{exc} values and the corresponding τ_{exc} and μ_{TL} values, assuming a thickness $d_{TL} = 20$ nm for the transport layer. The S_{exc} values for samples 1–3 (PTAA-PCBM/BCP and PTAA-PCBM:CMC:ICBA/BCP) lie between 1 and 40 cm/s, with corresponding τ_{exc} values approximately between 0.8 and 12 μs, while samples 4 and 5 (PTAA-C$_{60}$/BCP) show S_{exc} values between 20 and 100 cm/s with corresponding τ_{exc} values between 0.3 and 1 μs. The calculated transport layer mobilities for samples 1–3 lie between 10^{-4} and 3×10^{-3} cm^2 V^{-1} s^{-1}, similar to those reported in Refs. [15–17] for PTAA and PCBM layers. The faster charge

exchange lifetime and corresponding higher transport layer mobility of sample 3, compared to samples 1 and 2, is reflected in the higher fill factor of sample 3 compared to samples 1 and 2 (see Table S1 within the Supplemental Material [48]).

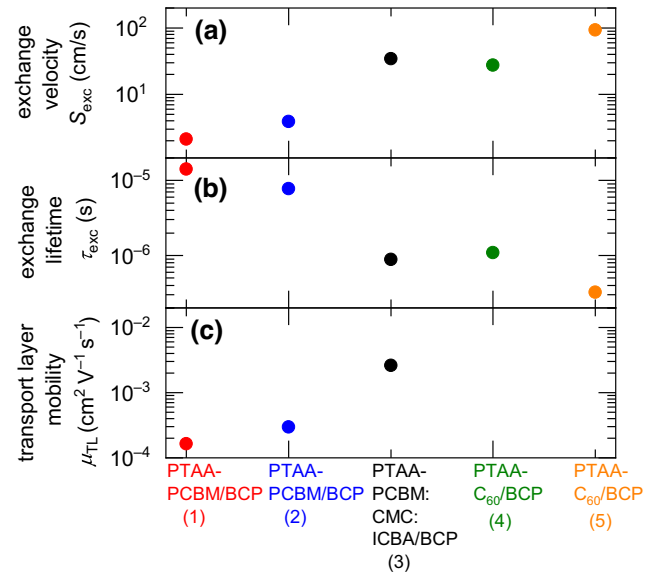In summary, we have developed an advanced model that captures the different physical mechanisms that contribute

FIG. 11. Calculated charge carrier (a) exchange velocity S_{exc}, (b) exchange lifetime τ_{exc} and transport layer mobilities for samples 1–5 from the experimental IS data measured at 1-sun open-circuit conditions in Fig. 1, which correspond to the PTAA-PCBM/BCP, PTAA-PCBM:CMC:ICBA/BCP, and PTAA-C$_{60}$/BCP combination of transport layers. Transport layer thickness $d_{TL} = 20$ nm is assumed to calculate the transport layer mobilities in (c). Light source used for the IS measurements is a blue LED centered at 482 nm.

to the frequency domain response of the PSC. This model focusses on the role of charge carrier exchange between the perovskite layer and the electrodes through the transport layers, and its coupling with recombination in the perovskite layer. The model identifies that the measured time constants of the PSC in a frequency domain measurement need not necessarily be limited by recombination but can also be limited by the resistance of the low-mobility transport layers. While discriminating between recombination-limited time constants and transport-layer-limited time constants is difficult due to the characteristic S shape of the time constants in both cases, the model predicts the evolution of the effective resistances and capacitances versus dc parameters, which allows us to differentiate between the two situations. Thus, the model can be used to calculate fundamental parameters of the PSC operation, such as the Shockley-Read-Hall lifetime, the charge carrier exchange lifetime (or velocity), and the transport layer mobilities. The last two parameters allow the quality of the transport layers and their interfaces with the perovskite layer to be determined by quantifying their ability to extract charge efficiently, since the ratio of the charge carrier lifetime and the recombination lifetime determines recombination losses at short circuit and low forward bias [40].

VI. CONCLUSIONS

In any time domain or frequency domain measurement of a solar cell, recombination and transport mechanisms are superimposed. In the case of perovskite solar cells, these mechanisms include not only transport within the perovskite layer but also charge extraction from the perovskite to the transport layer, followed by transport within the transport layer, and subsequent collection by the electrode. Due to the large diffusion length of electronic carriers in the perovskite layer, the charge extraction and transport properties of the transport layers are significant factors that determine the charge collection efficiency of the perovskite solar cell. While models that account for charge transport within the absorber layer exist in the literature, there is a lack of knowledge in the photovoltaic community regarding the physical mechanisms that govern charge extraction and collection, and their coupling with recombination in the perovskite layer.

To solve this problem, we develop a model for perovskite solar cells (and any multilayer solar cell in general) that describes the charge carrier exchange between the perovskite absorber and collecting electrodes through the transport layers, i.e., the conversion between internal and external voltages. The model predicts the influence of a charge carrier exchange lifetime that determines the rate at which charge carriers are injected into or extracted from the bulk volume of the absorber layer through the transport layers. This lifetime is associated with a charge carrier exchange resistance that models the potential drop across

the transport layers. For a variety of small-perturbation measurements in the frequency domain (IMVS, IMPS, and IS), we find that the additional information required to decouple recombination and charge carrier exchange is embedded in the voltage dependence of the time constants, which can be easily measured experimentally. With the help of drift-diffusion simulations, we explain the coupling between the different physical mechanisms that generate the expressed and unexpressed time constants, providing both analytical solutions and an equivalent circuit for the interpretation of experimental data.

In the case of impedance spectroscopy, the model predicts that, in cases where charge exchange is faster than the effective recombination lifetime, the typical S-shaped evolution of the measured time constants is observed. The voltage dependence of the time constants in such a scenario is dominated by the coupling between the recombination resistance and geometric capacitance at low open-circuit voltages, followed by a plateau corresponding to the SRH lifetime, and a subsequent exponentially voltage-dependent radiative lifetime at high open-circuit voltages. For cases where the charge carrier exchange is slower than the effective recombination lifetime, the time constant is dominated by the coupling between the charge carrier exchange resistance and the geometric capacitance, showing a characteristic exponential evolution at low open-circuit voltages and a plateau at higher open-circuit voltages. This plateau can be mistaken for a SRH recombination lifetime if the corresponding resistances and capacitances are not analyzed.

These insights are used to analyze impedance spectroscopy data of *p*-*i*-*n* perovskite solar cells with different transport layers. We find that the devices with the PTAA hole transport layer show the characteristic behavior and evolution of the charge carrier exchange resistance versus open-circuit voltage, irrespective of the type of electron transport layer used. This allows the determination of charge carrier exchange velocities between 1 and 100 cm/s under 1-sun open-circuit conditions, which corresponds to transport layer mobilities between 10^{-4} and 3×10^{-3} cm^2 V^{-1} s^{-1} for the PTAA-based PSCs.

S.R. carried out all the experiments, simulations, and wrote the first draft and the final version of the manuscript. Z.L. and Y.W. fabricated the samples. U.R. developed the concept of the charge carrier exchange model and contributed to the writing of the manuscript. T.K. supervised the project and contributed to reviewing and editing the manuscript.

There are no conflicts of interest to declare.

———

[1] S. Wheeler, D. Bryant, J. Troughton, T. Kirchartz, T. Watson, J. Nelson, and J. R. Durrant, Transient optoelectronic analysis of the impact of material energetics and recombination kinetics on the open-circuit voltage of hybrid perovskite solar cells, J. Phys. Chem. C **121**, 13496 (2017).

[2] D. W. de Quilettes, S. M. Vorpahl, S. D. Stranks, H. Nagaoka, G. E. Eperon, M. E. Ziffer, H. J. Snaith, and D. S. Ginger, Impact of microstructure on local carrier lifetime in perovskite solar cells, Science **348**, 683 (2015).

[3] J. Chung, S. S. Shin, K. Hwang, G. Kim, K. W. Kim, D.-S. Lee, W. Kim, B. S. Ma, Y.-K. Kim, T.-S. Kim, *et al.*, Record-efficiency flexible perovskite solar cell and module enabled by a porous-planar structure as an electron transport layer, Energy Environ. Sci. **13**, 4854 (2020).

[4] B. C. O'Regan, K. Bakker, J. Kroeze, H. Smit, P. Sommeling, and J. R. Durrant, Measuring charge transport from transient photovoltage rise times. A new tool to investigate electron transport in nanoparticle films, J. Phys. Chem. B **110**, 17155 (2006).

[5] L. Krückemeier, B. Krogmeier, Z. Liu, U. Rau, and T. Kirchartz, Understanding transient photoluminescence in halide perovskite layer stacks and solar cells, Adv. Energy Mater. **11**, 2003489 (2021).

[6] B. Krogmeier, F. Staub, D. Grabowski, U. Rau, and T. Kirchartz, Quantitative analysis of the transient photoluminescence of $CH_3NH_3PbI_3/PC_{61}BM$ heterojunctions by numerical simulations, Sustain. Energy Fuels **2**, 1027 (2018).

[7] L. Krückemeier, Z. Liu, B. Krogmeier, U. Rau, and T. Kirchartz, Consistent interpretation of electrical and optical transients in halide perovskite layers and solar cells, Adv. Energy Mater. **11**, 2102290 (2021).

[8] D. Kiermasch, A. Baumann, M. Fischer, V. Dyakonov, and K. Tvingstedt, Revisiting lifetimes from transient electrical characterization of thin film solar cells; a capacitive concern evaluated for silicon, organic and perovskite devices, Energy Environ. Sci. **11**, 629 (2018).

[9] S. Ravishankar, C. Aranda, S. Sanchez, J. Bisquert, M. Saliba, and G. Garcia-Belmonte, Perovskite solar cell modeling using light-and voltage-modulated techniques, J. Phys. Chem. C **123**, 6444 (2019).

[10] A. O. Alvarez, S. Ravishankar, and F. Fabregat-Santiago, Combining modulated techniques for the analysis of photosensitive devices, Small Methods **5**, 2100661 (2021).

[11] J. S. Laird, S. Ravishankar, K. J. Rietwyk, W. Mao, U. Bach, and T. A. Smith, Intensity modulated photocurrent microspectroscopy for next generation photovoltaics, Small Methods **6**, 2200493 (2022).

[12] A. Bou, H. Āboliņš, A. Ashoka, H. Cruanyes, A. Guerrero, F. Deschler, and J. Bisquert, Extracting *in situ* charge carrier diffusion parameters in perovskite solar cells with light modulated techniques, ACS Energy Lett. **6**, 2248 (2021).

[13] L. M. Herz, Charge-carrier mobilities in metal halide perovskites: Fundamental mechanisms and limits, ACS Energy Lett. **2**, 1539 (2017).

[14] Z. Liu, J. Siekmann, B. Klingebiel, U. Rau, and T. Kirchartz, Interface optimization via fullerene blends enables open-circuit voltages of 1.35 V in $CH_3NH_3Pb(I_{0.8}Br_{0.2})_3$ solar cells, Adv. Energy Mater. **11**, 2003386 (2021).

[15] S. Barard, M. Heeney, L. Chen, M. Cölle, M. Shkunov, I. McCulloch, N. Stingelin, M. Philips, and T. Kreouzis, Separate charge transport pathways determined by the time of flight method in bimodal polytriarylamine, J. Appl. Phys. **105**, 013701 (2009).

[16] E. Von Hauff, V. Dyakonov, and J. Parisi, Study of field effect mobility in PCBM films and P3HT:PCBM blends, Sol. Energy Mater. Sol. Cells **87**, 149 (2005).

[17] F. Steiner, S. Foster, A. Losquin, J. Labram, T. D. Anthopoulos, J. M. Frost, and J. Nelson, Distinguishing the influence of structural and energetic disorder on electron transport in fullerene multi-adducts, Mater. Horiz. **2**, 113 (2015).

[18] S. Ravishankar, Z. Liu, U. Rau, and T. Kirchartz, Multilayer Capacitances: How Selective Contacts Affect Capacitance Measurements of Perovskite Solar Cells, PRX Energy **1**, 013003 (2022).

[19] J. Siekmann, S. Ravishankar, and T. Kirchartz, Apparent defect densities in halide perovskite thin films and single crystals, ACS Energy Lett. **6**, 3244 (2021).

[20] S. Ravishankar, T. Unold, and T. Kirchartz, Comment on "resolving spatial and energetic distributions of trap states in metal halide perovskite solar cells", Science **371**, eabd8014 (2021).

[21] O. Breitenstein, An alternative one-diode model for illuminated solar cells, IEEE J. Photovoltaics **4**, 899 (2014).

[22] D. Grabowski, Z. Liu, G. Schöpe, U. Rau, and T. Kirchartz, Fill factor losses and deviations from the superposition principle in lead halide perovskite solar cells, Sol. RRL **6**, 2200507 (2022).

[23] U. Rau, V. Huhn, and B. E. Pieters, Luminescence Analysis of Charge-Carrier Separation and Internal Series-Resistance Losses in Cu(In, Ga)Se_2 Solar Cells, Phys. Rev. Appl. **14**, 014046 (2020).

[24] H. Wang, A. Guerrero, A. Bou, A. M. Al-Mayouf, and J. Bisquert, Kinetic and material properties of interfaces governing slow response and long timescale phenomena in perovskite solar cells, Energy Environ. Sci. **12**, 2054 (2019).

[25] T. Y. Yang, G. Gregori, N. Pellet, M. Grätzel, and J. Maier, The significance of ion conduction in a hybrid

organic–inorganic lead-iodide-based perovskite photosensitizer, Angew. Chem. **127**, 8016 (2015).

[26] D. V. Amasev, V. G. Mikhalevich, A. R. Tameev, S. R. Saitov, and A. G. Kazanskii, Formation of a two-phase structure in $CH_3NH_3PbI_3$ organometallic perovskite, Semiconductors **54**, 654 (2020).

[27] Z. Liu, L. Kruckemeier, B. Krogmeier, B. Klingebiel, J. A. Márquez, S. Levcenko, S. Öz, S.Mathur, U. Rau, T. Unold *et al.*, Open-circuit voltages exceeding 1.26 V in planar methylammonium lead iodide perovskite solar cells, ACS Energy Lett. **4**, 110 (2019).

[28] Z. S. Wang, F. Ebadi, B. Carlsen, W. C. Choy, and W. Tress, Transient photovoltage measurements on perovskite solar cells with varied defect concentrations and inhomogeneous recombination rates, Small Methods **4**, 2000290 (2020).

[29] J. Bisquert, Interpretation of the recombination lifetime in halide perovskite devices by correlated techniques, J. Phys. Chem. Lett. **13**, 7320 (2022).

[30] F. Fabregat-Santiago, J. Bisquert, G. Garcia-Belmonte, G. Boschloo, and A. Hagfeldt, Influence of electrolyte in transport and recombination in dye-sensitized solar cells studied by impedance spectroscopy, Sol. Energy Mater. Sol. Cells **87**, 117 (2005).

[31] S. J. Robinson, A. G. Aberle, and M. A. Green, Departures from the principle of superposition in silicon solar cells, J. Appl. Phys. **76**, 7920 (1994).

[32] T. Trupke, E. Pink, R. A. Bardos, and M. D. Abbott, Spatially resolved series resistance of silicon solar cells obtained from luminescence imaging, Appl. Phys. Lett. **90**, 093506 (2007).

[33] D. Lübke, P. Hartnagel, M. Hülsbeck, and T. Kirchartz, Understanding the thickness and light-intensity dependent performance of green-solvent processed organic solar cells, ACS Mater. Au **3**, 215 (2023).

[34] M. Stolterfoht, V. M. Le Corre, M. Feuerstein, P. Caprioglio, L. J. A. Koster, and D. Neher, Voltage-dependent photoluminescence and how it correlates with the fill factor and open-circuit voltage in perovskite solar cells, ACS Energy Lett. **4**, 2887 (2019).

[35] O. J. Sandberg, J. Kurpiers, M. Stolterfoht, D. Neher, P. Meredith, S. Shoaee, and A. Armin, On the question of the need for a built-in potential in perovskite solar cells, Adv. Mater. Interfaces **7**, 2000041 (2020).

[36] P. H. Nguyen, S. Scheinert, S. Berleb, W. Brütting, and G. Paasch, The influence of deep traps on transient current-voltage characteristics of organic light-emitting diodes, Org. Electron. **2**, 105 (2001).

[37] C. Stavrakas, G. Delport, A. A. Zhumekenov, M. Anaya, R. Chahbazian, O. M. Bakr, E. S. Barnard, and S. D. Stranks, Visualizing buried local carrier diffusion in halide perovskite crystals via two-photon microscopy, ACS Energy Lett. **5**, 117 (2020).

[38] W. Tian, C. Zhao, J. Leng, R. Cui, and S. Jin, Visualizing carrier diffusion in individual single-crystal organolead halide perovskite nanowires and nanoplates, J. Am. Chem. Soc. **137**, 12458 (2015).

[39] J. Bisquert, Chemical capacitance of nanostructured semiconductors: Its origin and significance for nanocomposite solar cells, Phys. Chem. Chem. Phys. **5**, 5360 (2003).

[40] L. Krückemeier, Z. Liu, T. Kirchartz, and U. Rau, Quantifying charge extraction and recombination using the rise and decay of the transient photovoltage of perovskite solar cells, Adv. Mater. 2300872 (2023).

[41] J. Bisquert and F. Fabregat-Santiago, in *Dye-Sensitized Solar Cells*, edited by K. Kalyanasundaram (EPFL Press, New York, 2010), Ch. 12.3.3.

[42] S. Ravishankar, L. Kruppa, S. Jenatsch, and Y. Wang, Discerning rise time constants to quantify charge carrier extraction in perovskite solar cells, Res. Sq. (2023), Preprint.

[43] E. Ponomarev and L. Peter, A generalized theory of intensity modulated photocurrent spectroscopy (IMPS), J. Electroanal. Chem. **396**, 219 (1995).

[44] L. Dloczik, O. Ileperuma, I. Lauermann, L. Peter, E. Ponomarev, G. Redmond, N. Shaw, and I. Uhlendorf, Dynamic response of dye-sensitized nanocrystalline solar cells: Characterization by intensity-modulated photocurrent spectroscopy, J. Phys. Chem. B **101**, 10281 (1997).

[45] O. J. Sandberg, K. Tvingstedt, P. Meredith, and A. Armin, Theoretical perspective on transient photovoltage and charge extraction techniques, J. Phys. Chem. C **123**, 14261 (2019).

[46] P. Hartnagel, S. Ravishankar, B. Klingebiel, O. Thimm, and T. Kirchartz, Comparing methods of characterizing energetic disorder in organic solar cells, Adv. Energy Mater 2300329 (2023).

[47] J. J. Haddad, B. Krogmeier, B. Klingebiel, L. Krückemeier, S. Melhem, Z. Liu, J. Hüpkes, S. Mathur, and T. Kirchartz, Analyzing interface recombination in lead-halide perovskite solar cells with organic and inorganic hole-transport layers, Adv. Mater. Interfaces **7**, 2000366 (2020).

[48] See the Supplemental Material http://link.aps.org/supplemental/10.1103/PRXEnergy.2.033006 for experimental details, derivation of the exchange current in terms of the perovskite-transport layer interface concentration, an extended derivation of the charge carrier exchange model, a derivation of the equivalent circuit from a charge carrier exchange model, a discussion of the simulation parameters, the effective resistance and capacitance of the equivalent circuit, a derivation of the SRH plateau width ΔV_{sat}, Figs. S1–S15 and Tables S1–S5. References [49–53] are also included.

[49] W. Shockley and W. Read Jr, Statistics of the recombinations of electrons and holes, Phys. Rev. **87**, 835 (1952).

[50] S. Sami, P. A. Haase, R. Alessandri, R. Broer, and R. W. Havenith, Can the dielectric constant of fullerene derivatives be enhanced by side-chain manipulation? A predictive first-principles computational study, J. Phys. Chem. A **122**, 3919 (2018).

[51] M. Sendner, Pabitra K. Nayak, David A. Egger, Sebastian Beck, Christian Müller, Bernd Epding, Wolfgang Kowalsky, Leeor Kronik, Henry J. Snaith, Annemarie Pucci and Robert Lovrinčić, Optical phonons in methylammonium lead halide perovskites and implications for charge transport, Mater. Horiz. **3**, 613 (2016).

[52] J. Maibach, E. Mankel, T. Mayer, and W. Jaegermann, The band energy diagram of PCBM-DH6T bulk

heterojunction solar cells: Synchrotron-induced photoelectron spectroscopy on solution processed DH6T:PCBM blends and *in situ* prepared PCBM/DH6T interfaces, J. Mater. Chem. C **1**, 7635 (2013).

[53] F. Staub, H. Hempel, J.-C. Hebig, J. Mock, U. W. Paetzold, U. Rau, T. Unold, and T. Kirchartz, Quantitative Analysis of the Transient Photoluminescence of $CH_3NH_3PbI_3/PC_{61}BM$ Heterojunctions by Numerical Simulations, Phys. Rev. Appl. **6**, 044017 (2016).

[54] Scripts for all MATLAB and SETFOS simulations are uploaded to the Zenodo database with the identifier 10.5281/zenodo.8076225.